

7 SCIENTIFIC HIGHLIGHT OF THE MONTH: "Electronic structure calculations with GPAW: A real-space implementation of the projector augmented-wave method"

J. Enkovaara^{1*}, C. Rostgaard², J. J. Mortensen^{2†}, J. Chen², M. Duřak², L. Ferrighi³, J. Gavnholt⁴, C. Glinsvad², V. Haikola⁵, H. A. Hansen², H. H. Kristoffersen³, M. Kuisma⁶, A. H. Larsen², L. Lehtovaara⁵, M. Ljungberg⁷, O. Lopez-Acevedo⁸, P. G. Moses², J. Ojanen⁶, T. Olsen⁴, V. Petzold², N. A. Romero⁹, J. Stausholm³, M. Strange², G. A. Tritsarlis², M. Vanin², M. Walter¹⁰, B. Hammer³, H. Häkkinen⁸, G. K. H. Madsen¹¹, R. M. Nieminen⁵, J. K. Nørskov², M. Puska⁵, T. Rantala⁶, J. Schiøtz⁴, K. S. Thygesen², K. W. Jacobsen²

¹CSC - IT Center for Science Ltd. P.O. Box 405 FI-02101 Espoo, Finland

²Center for Atomic-scale Materials Design, Department of Physics, Technical University of Denmark, DK-2800 Kgs. Lyngby, Denmark

³Interdisciplinary Nanoscience Center (iNANO) and Department of Physics and Astronomy, Aarhus University, DK-8000 Aarhus C, Denmark

⁴Danish National Research Foundation's Center for Individual Nanoparticle Functionality (CINF), Technical University of Denmark, DK-2800 Kgs. Lyngby, Denmark

⁵Department of Applied Physics, Aalto University School of Science and Technology, P.O.Box 11000, FIN-00076 Aalto, Espoo, Finland

⁶Department of Physics, Tampere University of Technology, P.O. Box 692, FI-33101 Tampere, Finland

⁷FYSIKUM, Stockholm University, Albanova University Center, SE-10691 Stockholm, Sweden

⁸Departments of Physics and Chemistry, Nanoscience Center, University of Jyväskylä, P.O. Box 35 (YFL), FI-40014 Finland

⁹Leadership Computing Facility, Argonne National Laboratory, Argonne, IL, USA

¹⁰Freiburg Materials Research Center, Stefan-Meier-Strasse 21, 79104 Freiburg, Germany

¹¹ICAMS, Ruhr Universität Bochum, 44801 Bochum, Germany

Abstract

Electronic structure calculations have become an indispensable tool in many areas of materials science and quantum chemistry. Even though the Kohn-Sham formulation of

*Corresponding author: jussi.enkovaara@csc.fi

†Corresponding author: jensj@fysik.dtu.dk

the density-functional theory (DFT) simplifies the many-body problem significantly, one is still confronted with several numerical challenges. In this article we present the projector augmented-wave (PAW) method as implemented in the GPAW program package[‡] using a uniform real-space grid representation of the electronic wave functions. Compared to more traditional plane wave or localized basis set approaches, real-space grids offer several advantages, most notably good computational scalability and systematic convergence properties. Additionally, as localized orbitals provide a conveniently small basis, we have also implemented the PAW method using atom-centered orbital basis sets. While DFT allows one to study ground state properties, time-dependent density-functional theory (TDDFT) provides access to the excited states. We have implemented the two common formulations of TDDFT, namely the linear-response and the time propagation schemes. Electron transport calculations under finite-bias conditions can be performed with GPAW using non-equilibrium Green functions and the localized basis set. In addition to the basic features of the real-space PAW method, we also describe the implementation of selected exchange-correlation functionals, parallelization schemes, Δ SCF-method, X-ray absorption spectra, and maximally localized Wannier orbitals.

1 Introduction

Electronic structure calculations have become an indispensable tool for simulations of condensed matter systems. Nowadays systems ranging from atoms and small molecules to nanostructures with several hundreds of atoms are studied routinely with density-functional theory (DFT) [1, 2].

In principle, only ground state properties such as total energies and equilibrium geometries can be investigated with DFT. However, several interesting material properties like excitation energies and optical spectra are related to the excited states of a system. These excited-state properties can be studied with time-dependent density-functional theory (TDDFT) [3].

Even though the DFT equations are much easier to solve than the full many-body Schrödinger equation, several numerical approximations are usually made. The approximations can be related to the treatment of core electrons and the region near the atomic nuclei (pseudopotential vs. all-electron methods) [4–8] or to the discretization of equations (plane-waves, localized orbitals, real-space grids, finite elements) [9–19]. In this work, we present a real-space-based implementation of the projector augmented-wave (PAW) method in the open source program package GPAW [20]. We note that there are several software packages that currently implement the PAW method using a plane-wave basis [21–23].

The PAW method [7, 24] is formally an all-electron method which provides an exact transformation between the smooth pseudo wave functions and the all-electron wave functions. While in practical implementations the PAW method resembles pseudopotential methods, it addresses several shortcomings of norm-conserving or ultrasoft pseudopotentials. The PAW method offers a reliable description over the whole periodic table with good

[‡]<https://wiki.fysik.dtu.dk/gpaw>

transferability of PAW potentials. The pseudo wave functions in the PAW method are typically smoother compared to norm-conserving pseudopotential methods so that the wave functions can be represented with fewer degrees of freedom. The PAW approximation contains all the information about the nodal structure of wave functions near the nuclei, and it is always possible to reconstruct the all-electron wave functions from the pseudo wave functions.

In the solid state community, plane-wave basis sets [9, 22, 25, 26] are the most popular choice for discretizing the density-functional equations while localized basis sets [11, 27] have been more popular in quantum chemistry. A more recent approach is the use of uniform real-space grids [13, 28–30]. Real-space methods provide several advantages over plane waves. A plane-wave basis imposes periodic boundary conditions, while a real-space grid can flexibly treat both free and periodic boundary conditions. The plane-wave method relies heavily on fast Fourier transforms which are difficult to parallelize efficiently due to the non-local nature of the operations. On the other hand, in real space it is possible to work entirely with local and semi-local operations which enables efficient parallelization with small communication overhead. The accuracy of a real-space representation can be increased systematically by decreasing the grid spacing, similar to increasing the kinetic energy cut-off in a plane wave calculation. This systematic improvement of accuracy is also the main advantage of both real-space and plane-wave methods compared to localized basis sets, where the accuracy of representation cannot be controlled as systematically. However, as localized functions can provide a very compact basis set, we have implemented also atom-centered basis functions for situations where the high accuracy of a real-space grid is not needed. The atom-centered basis is especially convenient in the context of electron transport calculations within the non-equilibrium Green function approach also implemented in GPAW. To our knowledge, GPAW is the first publicly available package to implement the PAW method with uniform real-space grids and atom-centered localized orbitals.

In tandem with numerical approximations, physical approximations are needed in DFT since the exact form of the exchange-correlation (XC) functional is unknown. The traditional local density and generalized gradient approximations have been surprisingly successful, but due to well-known shortcomings, there are continuing efforts to go beyond them. Some of the new developments in this field, such as meta-GGA and exact-exchange based approximations are available in GPAW.

Time-dependent density-functional theory (TDDFT) can be realized in two different formalism. In the most general form, the time-dependent Kohn-Sham equations are integrated over the time-domain [31]. In the linear-response regime it is also possible to obtain excitation energies by solving a matrix equation in an electron-hole basis [32]. The real-time propagation and the linear-response approaches are complementary. For example, the linear-response scheme provides all the excitations in a single calculation, while the real-time formalism provides the excitations corresponding to a given initial perturbation. On the other hand, the real-time propagation scheme can address also non-linear effects.

While the linear-response scheme is more efficient for small systems, the real-time propagation approach scales more favorably with system size. Both the linear-response and real-time forms are implemented in GPAW, to our knowledge for the first time within the PAW method.

In addition to the standard total energy calculations, GPAW contains several more specific features. For example, excitation energies can be estimated with the Δ SCF method [33] as an alternative to the TDDFT approaches. X-ray absorption spectra and maximally localized Wannier functions can also be calculated.

This article is organized as follows: First, the general features of the PAW method and the implementation on a real-space grid are described in Sec. 2. In Sec. 3 we give an overview of the different exchange-correlation functionals available, and in Sec. 4 we discuss a recent method for error estimations within DFT. An overview of TDDFT is presented in Sec. 5, and the localized basis set and its use in finite bias transport calculations are described in Sec. 6. In Sec. 7 other features, such as Δ SCF, X-ray absorption spectra and Wannier functions are described. The parallelization strategy and parallel scaling are presented in Sec. 8. Finally, we provide a summary and an outlook in Sec. 9.

2 General overview

In this section, we present the main features of our PAW implementation. Some of the details have been published earlier [34], so we provide here a general overview and discuss in more detail only the parts where our approach has changed from the earlier publication. The notation is similar to the one used in the original references [7]. We use Hartree atomic units ($\hbar = m = e = \frac{4\pi}{\epsilon_0} = 1$) throughout the article. Generally, the equations are written for the case of a spin-paired and finite system of electrons and the spin and k-point indices are included when necessary.

2.1 Projector augmented-wave method

In the Kohn-Sham formulation of DFT, we work with single-particle all-electron wave functions to describe core, semi-core and valence states. The PAW method is a linear transformation between smooth valence (and semi-core) pseudo (PS) wave functions, $\tilde{\psi}_n$ (n is the state index) and all-electron (AE) wave functions, ψ_n . The core states of the atoms, $\phi_i^{a,\text{core}}$, are fixed to the reference shape for the isolated atom. Here a is an atomic index and i is a combination index for the principal, angular momentum, and magnetic quantum numbers respectively (n , ℓ and m).

Given a smooth PS wave function, the corresponding AE wave function, which is orthogonal to the set of $\phi_i^{a,\text{core}}$ orbitals, can be obtained through a linear transformation

$$\psi_n(\mathbf{r}) = \hat{\mathcal{T}}\tilde{\psi}_n(\mathbf{r}). \quad (1)$$

The transformation operator, $\hat{\mathcal{T}}$, is given in terms of atom-centered AE partial waves,

$\phi_i^a(\mathbf{r})$, the corresponding smooth partial waves, $\tilde{\phi}_i^a(\mathbf{r})$, and projector functions, $\tilde{p}_i^a(\mathbf{r})$, as

$$\hat{\mathcal{T}} = 1 + \sum_a \sum_i (|\phi_i^a\rangle - |\tilde{\phi}_i^a\rangle) \langle \tilde{p}_i^a|, \quad (2)$$

where atom a is at the position \mathbf{R}^a . The defining properties of the atom-centered functions are that AE partial waves and smooth PS partial waves are equal outside atom-centered augmentation spheres of radii r_c^a ,

$$\phi_i^a(\mathbf{r}) = \tilde{\phi}_i^a(\mathbf{r}), \quad |\mathbf{r} - \mathbf{R}^a| > r_c^a \quad (3)$$

and that the projector functions are localized inside the augmentation spheres and are orthogonal to the PS partial waves

$$\langle \tilde{p}_{i_1}^a | \tilde{\phi}_{i_2}^a \rangle = \delta_{i_1 i_2}. \quad (4)$$

In principle, an infinite number of atom-centered partial waves and projectors is required for the PAW transformation to be exact. However, in practical calculations it is usually enough to include one or two functions per angular momentum channel. The projectors and partial waves are constructed from an AE calculation for a spherically symmetric atom.

Inside the augmentation sphere of atom a , we can define one-center expansions of an AE and PS state as [7]

$$\psi_n^a(\mathbf{r}) = \sum_i P_{in}^a \phi_i^a(\mathbf{r}) \quad (5)$$

and

$$\tilde{\psi}_n^a(\mathbf{r}) = \sum_i P_{in}^a \tilde{\phi}_i^a(\mathbf{r}), \quad (6)$$

where the expansion coefficients are

$$P_{in}^a = \langle \tilde{p}_i^a | \tilde{\psi}_n^a \rangle. \quad (7)$$

For a complete set of partial waves, we have $\psi_n = \psi_n^a$ and $\tilde{\psi}_n = \tilde{\psi}_n^a$ for $|\mathbf{r} - \mathbf{R}^a| < r_c^a$ which leads to

$$\psi_n = \tilde{\psi}_n + \sum_a (\psi_n^a - \tilde{\psi}_n^a). \quad (8)$$

Here, the term in the parenthesis is a correction inside the augmentation spheres only.

We define a PS electron density

$$\tilde{n}(\mathbf{r}) = \sum_n f_n |\tilde{\psi}_n(\mathbf{r})|^2 + \sum_a \tilde{n}_c^a(\mathbf{r}), \quad (9)$$

where f_n are occupation numbers between 0 and 2, and \tilde{n}_c^a is a smooth PS core density equal to the AE core density n_c^a outside the augmentation sphere. From the atomic density matrix $D_{i_1 i_2}^a$

$$D_{i_1 i_2}^a = \sum_n \langle \tilde{\psi}_n | \tilde{p}_{i_1}^a \rangle f_n \langle \tilde{p}_{i_2}^a | \tilde{\psi}_n \rangle. \quad (10)$$

we define one-center expansions of the AE and PS densities,

$$n^a(\mathbf{r}) = \sum_{i_1, i_2} D_{i_1 i_2}^a \phi_{i_1}^a(\mathbf{r}) \phi_{i_2}^a(\mathbf{r}) + n_c^a(\mathbf{r}), \quad (11)$$

and

$$\tilde{n}^a(\mathbf{r}) = \sum_{i_1, i_2} D_{i_1 i_2}^a \tilde{\phi}_{i_1}^a(\mathbf{r}) \tilde{\phi}_{i_2}^a(\mathbf{r}) + \tilde{n}_c^a(\mathbf{r}), \quad (12)$$

respectively.

From \tilde{n} , n^a and \tilde{n}^a , we can construct the AE density in terms of a smooth part and atom-centered corrections

$$n(\mathbf{r}) = \tilde{n}(\mathbf{r}) + \sum_a (n^a(\mathbf{r}) - \tilde{n}^a(\mathbf{r})). \quad (13)$$

The PAW total energy expression has three contributions: kinetic, Coulomb and XC energy, all of which are composed of a PS part and atomic corrections. For the kinetic energy, we get

$$\tilde{E}_{\text{kin}} = -\frac{1}{2} \sum_n f_n \int d\mathbf{r} \tilde{\psi}_n(\mathbf{r}) \nabla^2 \tilde{\psi}_n(\mathbf{r}), \quad (14)$$

$$\begin{aligned} \Delta E_{\text{kin}}^a &= -\frac{1}{2} 2 \sum_i^{\text{core}} \int d\mathbf{r} \phi_i^a(\mathbf{r}) \nabla^2 \phi_i^a(\mathbf{r}) \\ &\quad - \frac{1}{2} \sum_{i_1 i_2} D_{i_1 i_2}^a \int d\mathbf{r} \left(\phi_{i_1}^a(\mathbf{r}) \nabla^2 \phi_{i_2}^a(\mathbf{r}) - \tilde{\phi}_{i_1}^a(\mathbf{r}) \nabla^2 \tilde{\phi}_{i_2}^a(\mathbf{r}) \right). \end{aligned} \quad (15)$$

Before we can write down the expression for the PAW Coulomb energy, we must define one-center AE and PS charge densities

$$\rho^a(\mathbf{r}) = n^a(\mathbf{r}) - Z^a \delta(\mathbf{r} - \mathbf{R}^a), \quad (16)$$

$$\tilde{\rho}^a(\mathbf{r}) = \tilde{n}^a(\mathbf{r}) + \sum_{\ell m} Q_{\ell m}^a \hat{g}_{\ell m}^a(\mathbf{r}), \quad (17)$$

where Z^a is the atomic number of atom a , $\hat{g}_{\ell m}^a(\mathbf{r}) = \hat{g}_\ell^a(|\mathbf{r} - \mathbf{R}^a|) Y_{\ell m}(\mathbf{r} - \mathbf{R}^a)$ is a shape function localized inside the augmentation sphere fulfilling $\int r^2 dr r^\ell \hat{g}_\ell^a(r) = 1$ and $Q_{\ell m}^a$ are multipole moments that we choose as described below. We define a PS charge density as

$$\tilde{\rho}(\mathbf{r}) = \tilde{n}(\mathbf{r}) + \sum_a \sum_{\ell m} Q_{\ell m}^a \hat{g}_{\ell m}^a(\mathbf{r}), \quad (18)$$

so that the AE charge density is $\rho = \tilde{\rho} + \sum_a (\rho^a - \tilde{\rho}^a)$. By choosing $Q_{\ell m}^a$ so that ρ^a and $\tilde{\rho}^a$ have the same multipole moments, augmentation spheres on different atoms will be electrostatically decoupled and the Coulomb energy is simply

$$\tilde{E}_{\text{coul}} = \frac{1}{2} \int d\mathbf{r} d\mathbf{r}' \frac{\tilde{\rho}(\mathbf{r}) \tilde{\rho}(\mathbf{r}')}{|\mathbf{r} - \mathbf{r}'|}, \quad (19)$$

$$\Delta E_{\text{coul}}^a = \frac{1}{2} \int d\mathbf{r} d\mathbf{r}' \frac{\rho^a(\mathbf{r}) \rho^a(\mathbf{r}') - \tilde{\rho}^a(\mathbf{r}) \tilde{\rho}^a(\mathbf{r}')}{|\mathbf{r} - \mathbf{r}'|}. \quad (20)$$

For local and semi-local XC-functionals, the contributions to the XC energy is

$$\tilde{E}_{\text{xc}} = E_{\text{xc}}[\tilde{n}], \quad (21)$$

$$\Delta E_{\text{xc}}^a = E_{\text{xc}}[n^a] - E_{\text{xc}}[\tilde{n}^a]. \quad (22)$$

There is one extra term in the PAW total energy expression which does not have a physical origin

$$\tilde{E}_{\text{zero}} = \int d\mathbf{r} \tilde{n}(\mathbf{r}) \sum_a \bar{v}^a(\mathbf{r}), \quad (23)$$

$$\Delta E_{\text{zero}}^a = - \int d\mathbf{r} \tilde{n}^a(\mathbf{r}) \bar{v}^a(\mathbf{r}). \quad (24)$$

The only restriction in the choice of the so called zero-potential (or local potential) \bar{v}^a is that it must be zero outside the augmentation sphere of atom a . For a complete set of partial waves and projectors, $\tilde{E}_{\text{zero}} + \sum_a \Delta E_{\text{zero}}^a$ is exactly zero, but for practical calculations with a finite number of partial waves and projector functions, \bar{v}^a can be used to improve the accuracy of a PAW calculation [35].

The final expression for the energy is

$$E = \tilde{E} + \sum_a \Delta E^a \quad (25)$$

$$\begin{aligned} &= \tilde{E}_{\text{kin}} + \tilde{E}_{\text{coul}} + \tilde{E}_{\text{xc}} + \tilde{E}_{\text{zero}} \\ &+ \sum_a (\Delta E_{\text{kin}}^a + \Delta E_{\text{coul}}^a + \Delta E_{\text{xc}}^a + \Delta E_{\text{zero}}^a). \end{aligned} \quad (26)$$

The smooth PS wave functions $\tilde{\psi}_n$ are orthonormal only with respect to the PAW overlap operator \hat{S} : $\langle \tilde{\psi}_n | \hat{S} | \tilde{\psi}_m \rangle = \delta_{nm}$, where

$$\hat{S} = \hat{T}^\dagger \hat{T} = 1 + \sum_a \sum_{i_1 i_2} |\tilde{p}_{i_1}^a\rangle \Delta S_{i_1 i_2}^a \langle \tilde{p}_{i_2}^a|, \quad (27)$$

$$\Delta S_{i_1 i_2}^a = \langle \phi_{i_1}^a | \phi_{i_2}^a \rangle - \langle \tilde{\phi}_{i_1}^a | \tilde{\phi}_{i_2}^a \rangle. \quad (28)$$

This leads to the generalized eigenproblem

$$\hat{H} \tilde{\psi}_n = \epsilon_n \hat{S} \tilde{\psi}_n, \quad (29)$$

where

$$\hat{H} = -\frac{1}{2} \nabla^2 + \tilde{v} + \sum_a \sum_{i_1 i_2} |\tilde{p}_{i_1}^a\rangle \Delta H_{i_1 i_2}^a \langle \tilde{p}_{i_2}^a|, \quad (30)$$

$$\Delta H_{i_1 i_2}^a = \frac{\partial \Delta E^a}{\partial D_{i_1 i_2}^a} + \int d\mathbf{r} \tilde{v}_{\text{coul}}(\mathbf{r}) \frac{\partial \tilde{\rho}(\mathbf{r})}{\partial D_{i_1 i_2}^a}, \quad (31)$$

and the effective potential

$$\tilde{v} = \frac{\delta \tilde{E}}{\delta \tilde{n}} = \tilde{v}_{\text{coul}} + \tilde{v}_{\text{xc}} + \sum_a \bar{v}^a, \quad (32)$$

where the Coulomb potential satisfies the Poisson equation $\nabla^2 \tilde{v}_{\text{coul}} = -4\pi \tilde{\rho}$ and \tilde{v}_{xc} is the XC potential.

2.2 Atomic setups

For each type of atom, we construct an atomic setup consisting of the following quantities: ϕ_i^a , $\tilde{\phi}_i^a$, \tilde{p}_i^a , n_c^a , \tilde{n}_c^a , $\hat{g}_{\ell m}$, \bar{v}^a and r_c^a . From a reference calculation for the isolated neutral spin-paired spherically symmetric atom, we calculate the required AE partial waves ϕ_i^a and the core density n_c^a . We choose a cutoff radius r_c^a for the augmentation sphere and a shape for $\hat{g}_{\ell m}$, which is usually a Gaussian. The smooth PS partial waves $\tilde{\phi}_i^a$ and the smooth PS core density \tilde{n}_c^a are constructed by smooth continuation of ϕ_i^a and n_c^a , respectively, inside the augmentation sphere. The projector functions \tilde{p}_i^a are constructed as described in Ref. [7] and \bar{v}^a is chosen so that the effective potential \tilde{v} becomes as smooth as possible or to produce good scattering of f -states [35]. For more details, see Ref. [34].

All the functions in an atomic setup are of the form of a radial function times spherical harmonics and each radial function is tabulated on a radial grid. Since ϕ_i^a and n_c^a can contain tightly bound localized electrons, the radial grid used has a higher grid density close to $r = 0$ than further from the nucleus (we use $r_i = \beta i / (N - i)$ for $i = 0, 1, \dots, N$). All the functions comprising a setup need only be known for $r < r_c^a$ except for $\tilde{\phi}_i^a$ and \tilde{n}_c^a , which are used also for initialization of wave functions and density.

2.3 Uniform 3-d real-space grids

Uniform real-space grids provide a simple discretization for the Kohn-Sham and Poisson equations. Physical quantities such as wave functions, densities, and potentials are represented by the values at the grid points. Derivatives are calculated using finite differences. The accuracy of discretization is determined by the grid spacing and the finite difference approximations used for the derivatives.

For a general unit cell with lattice vectors \mathbf{a}_α ($\alpha = 1, 2, 3$) and N_α grid points along the three directions, we define grid spacing vectors $\mathbf{h}_\alpha = \mathbf{a}_\alpha / N_\alpha$. For an orthorhombic unit cell, the Laplacian is discretized as:

$$\nabla^2 f(\mathbf{r}) = \sum_{\alpha=1}^D \sum_{n=-N}^N b_\alpha c_n^N f(\mathbf{r} + n\mathbf{h}_\alpha) + O(h^{2N}), \quad (33)$$

where $D = 3$, $b_\alpha = 1/h_\alpha^2$ and c_n^N are the N^{th} order finite difference coefficients for the second derivative expansion.

In the case of a non-orthorhombic unit cell, we extend the set of grid spacing vectors with more nearest neighbor directions. The D coefficients b_α are determined by the conventional method of undetermined coefficients, inserting the six functions $f(\mathbf{r}) = x^2, y^2, z^2, xy, yz, zx$ in Eq. (33) and solving for b_α at $\mathbf{r} = (0, 0, 0)$. The number of directions needed to satisfy the six equations depends on the symmetry of the lattice: For hexagonal or body centered cubic symmetry, $D = 4$ directions are needed, while $D = 6$ directions are used for a face centered cubic cell or a general unit cell without any symmetry. This procedure allows for finite difference stencils with only $1 + 2DN$ points, which is similar to the stencils defined by Natan *et al.* [36].

It must be noted that the performance of a given stencil is to an extent structure-dependent. For example, for calculations of individual molecules, where large gradients are present, a more compact stencil may outperform a higher accuracy but less compact one. However, good accuracy is typically obtained for a combination of a grid spacing of $h = 0.2 \text{ \AA}$ and a finite difference stencil with $O(h^6)$ error for the kinetic energy.

The PS electron density is evaluated on the same grid as the wave functions. It is then interpolated to a finer grid with a grid spacing of $h/2$, where the XC energy and potential are calculated. The fine grid is also used for constructing the PS charge density and for solving the Poisson equation. The discretization of the Poisson equation is done with a finite-difference stencil like Eq. (33) with an error of $O(h^6)$. For orthorhombic unit cells a more compact Mehrstellen type stencil [16] can also be used for solving the Poisson equation. The effective potential, Eq. (32), is then restricted to the coarse grid where it can be applied to the wave functions.

Boundary conditions for the quantities represented on 3-d grids can be zero for an isolated system or periodic for a periodic system (or any combination). When using \mathbf{k} -point sampling, a wave function can also have Bloch type boundary conditions

$$\tilde{\psi}_{n\mathbf{k}}(\mathbf{r} + \mathbf{R}) = \tilde{\psi}_{n\mathbf{k}}(\mathbf{r})e^{i\mathbf{k}\cdot\mathbf{R}}, \quad (34)$$

where \mathbf{R} is any Bravais vector. For charged systems, the boundary condition for \tilde{v}_{coul} can be determined from a multipole expansion.

2.4 Localized functions and Fourier filtering

Special care is needed when dealing with integrals involving products of localized functions centered on an atom and functions spanning the whole simulation cell. As an example, consider the projection of a wave function onto a projector function $\tilde{p}_i^a(\mathbf{r}) = \tilde{p}_{n_i\ell_i}^a(|\mathbf{r} - \mathbf{R}^a|)Y_{\ell_i m_i}(\mathbf{r} - \mathbf{R}^a)$ centered on atom a . This integral is approximated by a sum over grid points:

$$\langle \tilde{p}_i^a | \tilde{\psi} \rangle = \sum_g \tilde{p}_i^a(\mathbf{r}_g) \tilde{\psi}(\mathbf{r}_g) \Delta v, \quad (35)$$

where Δv is the volume per grid point. In order to make the integration as accurate as possible, it is important that the radial function $\tilde{p}_{n_i\ell_i}^a(r)$ contains as few short-wavelength components as possible. To achieve this, we Fourier filter our projector functions using the mask-function technique [37]. Here, the radial function is divided by a mask function that goes smoothly to zero at approximately twice the original cutoff radius. We use $m(r) = \exp(-\gamma r^2)$. After a Fourier transform, the short wavelength components are cut off by multiplying the spectrum by a smooth cutoff function. Transforming back to real-space, the final result is obtained by multiplying by $m(r)$, which will remove the oscillating and decaying tail beyond the cutoff of the chosen mask function.

In the PAW formalism, there are four different types of localized functions that need to be evaluated on the grid points: projector functions \tilde{p}_i^a , the zero potential \tilde{v}^a , the shape functions $\hat{g}_{\ell m}^a$ (for the compensation charges), and the PS core density \tilde{n}_c^a ; we apply the

mask function technique to \tilde{p}_i^a and \bar{v}^a . The radial part of the shape functions are chosen as $r^\ell e^{-\alpha^a r^a}$ and are therefore optimally smooth [38], and the PS core densities can always be chosen very smooth.

2.5 Iterative solution of eigenproblem

The Hamiltonian and overlap operators appearing in the generalized eigenvalue problem Eq. (29) are large sparse matrices in the real-space grid representation. Due to the large size of the matrices, direct diagonalization schemes which scale $O(N^3)$ with the matrix size are not tractable. On the other hand, sparsity of the matrices makes iterative diagonalization schemes [9, 39] appealing due to their dominant $O(N^2)$ scaling.

We have implemented three different iterative eigensolvers which share some common ingredients: the residual minimization method-direct inversion in iterative subspace (RMM-DIIS) [39, 40], the conjugate gradient method [9, 41], and Davidson's method [39, 42]. A basic concept in all the methods is the update of the eigenvectors $\tilde{\psi}_n$ with the residuals

$$R_n = (\hat{H} - \epsilon_n \hat{S})\tilde{\psi}_n. \quad (36)$$

The convergence of iterative methods can be accelerated with preconditioning, and we calculate preconditioned residuals $\tilde{R}_n = \hat{P}R_n$, by solving approximately a Poisson equation

$$\frac{1}{2}\nabla^2 \tilde{R}_n = R_n \quad (37)$$

with a multigrid method [16].

A subspace diagonalization is always performed before the iteration steps. The RMM-DIIS method does not conserve the orthonormality of eigenvectors, and thus explicit orthonormalization is done after each RMM-DIIS step. A good initial guess for the wave functions is especially important for the robustness of the RMM-DIIS algorithm. We take the initial guess from an atomic orbital basis calculation, the details of which are described in section 6.

2.6 Density mixing

During the self-consistency cycles both wave functions and the density are updated iteratively. New PS density $\tilde{n}(\mathbf{r})$ and atomic density matrices $D_{i_1 i_2}^a$ are calculated from the wave functions, Eqs. (9-10) and mixed with the old densities using Pulay's method [39, 43].

Pulay's method requires a good metric \hat{M} for measuring the change from input to output density $\langle \Delta \tilde{n} | \hat{M} | \Delta \tilde{n} \rangle$, where $\Delta \tilde{n} = \tilde{n}_{\text{out}} - \tilde{n}_{\text{in}}$, in order to determine the optimal linear combination of old output densities. It is important that \hat{M} puts more weight on long wavelength changes as these can introduce charge sloshing in systems with many states at the Fermi level. Ref. [39], for example, uses the metric

$$\hat{M} = \sum_q f_q |\mathbf{q}\rangle \langle \mathbf{q}|, \quad \text{with} \quad f_q = \frac{q^2 + q_1^2}{q^2}, \quad (38)$$

where $q_1 \sim 1$ and $|\mathbf{q}\rangle$ is a plane wave with wave vector \mathbf{q} . Expressed on a real-space grid where $|\mathbf{R}\rangle$ is a grid point at \mathbf{R} , we have

$$\hat{M} = \sum_{\mathbf{R}\mathbf{R}'} M_{\mathbf{R}\mathbf{R}'} |\mathbf{R}\rangle \langle \mathbf{R}'|, \quad \text{with} \quad M_{\mathbf{R}\mathbf{R}'} = \sum_{\mathbf{q}} f_q e^{i\mathbf{q}\cdot(\mathbf{R}'-\mathbf{R})}. \quad (39)$$

We would like to calculate scalar products from the density on the real space grid, but the non-locality of Eq. (39) makes this intractable. We therefore seek a more local metric \hat{M} , which can be represented as a finite difference operator

$$\hat{M} = \sum_{\mathbf{R}} \sum_{i=0}^N \sum_{\mathbf{v} \in \mathcal{V}_i} c_i |\mathbf{R}\rangle \langle \mathbf{R} + \mathbf{v}|, \quad (40)$$

where \mathcal{V}_i is the set of vectors pointing to the i th nearest neighbors of a grid point. We enforce \hat{M} to be semi-local by including only up to N th nearest neighbors. In reciprocal space \hat{M} has matrix elements

$$\tilde{f}_{\mathbf{q}} = \langle \mathbf{q} | \hat{M} | \mathbf{q}' \rangle = \sum_i c_i \sum_{\mathbf{v} \in \mathcal{V}_i} e^{i\mathbf{q}\cdot\mathbf{v}} \delta_{\mathbf{q},\mathbf{q}'}. \quad (41)$$

The coefficients c_i should be determined so that Eq. (41) mimics the behavior of f_q in Eq. (38). This means that $\tilde{f}_{\mathbf{q}}$ should decay monotonically from a weight factor $w > 1$ at $q = 0$ to 1 for the largest wave vectors at the zone boundary in reciprocal space: $\tilde{f}_{(\pi/h, q_y, q_z)}^{(3)} = 1$ for $|q_y| \leq \pi/h$ and $|q_z| \leq \pi/h$. For an orthorhombic grid with grid spacing h , including up to 3rd nearest neighbors, we can fulfill these boundary conditions with the coefficients

$$c_0 = \frac{w+7}{8}, \quad c_1 = \frac{w-1}{16}, \quad c_2 = \frac{w-1}{32}, \quad c_3 = \frac{w-1}{64}. \quad (42)$$

We find the metric to improve convergence significantly when there are many states near the Fermi level. A value of $w = 100$ seems to be a good choice.

3 Exchange-correlation functionals in GPAW

The exact form of the exchange-correlation (XC) functional in the DFT is not known. Thus, it has to be approximated, which constitutes the fundamental physical approximation in practical calculations. GPAW provides several forms of XC functionals ranging from the basic local density (LDA) and generalized gradient (GGA) approximations to the more exotic hybrid functionals; a van der Waals density functional and the Hubbard-corrected DFT+U are also available. For the basic functionals GPAW uses libxc [44] which is an open source library of popular XC functionals: LDA, GGA, and meta-GGA. The exchange and correlation parts of libxc can be freely combined. In the following we describe the more advanced functionals implemented in GPAW.

3.1 Meta-GGA

Meta-GGAs use the kinetic-energy density in addition to densities and density gradients in standard GGAs so that more of the known properties of the exact XC functional can be fulfilled [45]. The kinetic energy density is defined as

$$\tau(\mathbf{r}) = \frac{1}{2} \sum_n f_n |\nabla \psi_n(\mathbf{r})|^2. \quad (43)$$

The MGGAs currently implemented in GPAW [46–48] depend on the reduced (dimensionless) quantities τ/τ^{HEG} and τ/τ^{vW} , where

$$\tau^{\text{HEG}} = \frac{3}{10} (6\pi^2)^{2/3} n^{5/3} \quad (44)$$

is the kinetic energy density of the homogeneous electron gas (HEG), and

$$\tau^{\text{vW}} = \frac{|\nabla n|^2}{8n} \quad (45)$$

is the von Weizsäcker (vW) kinetic-energy density.

Just like the AE density, Eq. (13), the kinetic energy density can be written as $\tau = \tilde{\tau} + \sum_a (\tau^a - \tilde{\tau}^a)$, where the smooth part is

$$\tilde{\tau}(\mathbf{r}) = \frac{1}{2} \sum_n f_n |\nabla \tilde{\psi}_n(\mathbf{r})|^2 + \sum_a \tilde{\tau}_c^a(\mathbf{r}), \quad (46)$$

and the atom-centered parts are

$$\tau^a(\mathbf{r}) = \frac{1}{2} \sum_{i_1 i_2} D_{i_1 i_2}^a \nabla \phi_{i_1}(\mathbf{r}) \cdot \nabla \phi_{i_2}(\mathbf{r}) + \tau_c^a(r), \quad (47)$$

$$\tilde{\tau}^a(\mathbf{r}) = \frac{1}{2} \sum_{i_1 i_2} D_{i_1 i_2}^a \nabla \tilde{\phi}_{i_1}(\mathbf{r}) \cdot \nabla \tilde{\phi}_{i_2}(\mathbf{r}) + \tilde{\tau}_c^a(r). \quad (48)$$

The AE and PS core kinetic energy densities $\tau_c^a(r)$ and $\tilde{\tau}_c^a(r)$ are simple radial functions that are calculated during atomic setup generation.

Currently, GPAW enables calculation of non-self-consistent TPSS [46], revTPSS [48] and M06-L [47] energies. The use of PBE orbitals in a non-self-consistent calculations of atomization energies and bond lengths for small molecules has been determined to be accurate [49]. In Fig. 1 the GPAW atomization energies errors, with respect to experiments, are reported both for the PBE and MGGA functionals. The TPSS mean absolute error with respect to experimental values obtained with GPAW is 0.13 eV, and this is consistent with the value of 0.14 eV of Ref. [49]. All MGGA functionals employed improve over the PBE atomization energies whose mean absolute error is 0.33 eV.

3.2 Exact exchange

GPAW offers access to the Fock exchange energy (exact exchange), as well as fractional inclusion of the Fock operator in the hybrid XC functionals. The exact-exchange (EXX)

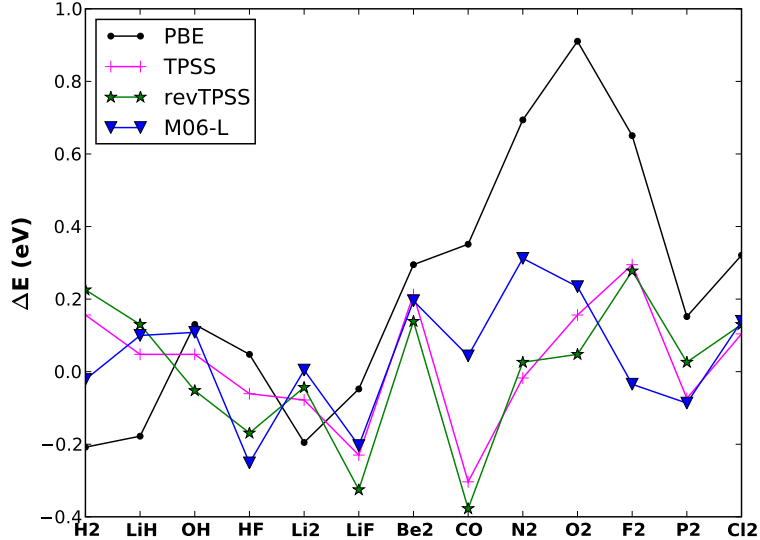


Figure 1: PBE, TPSS, revTPSS and M06-L non-self-consistent atomization energies errors, with respect to experiments, calculated with GPAW for small molecules, in eV. The MGGA GPAW values are obtained from PBE orbitals at experimental geometries. Experimental values are as in Ref. [49].

functional was implemented within the PAW method in a plane-wave basis [50], but to the authors' knowledge this is the first implementation in a real-space PAW method. As the PAW related expressions are independent of the basis, we refer to Ref. [50] for their derivation, and sketch only the main features here.

The EXX energy functional is given by

$$E_{\text{xx}} = -\frac{1}{2} \sum_{ij\sigma} f_{i\sigma} f_{j\sigma} K_{ij\sigma,ij\sigma}^C, \quad (49)$$

where i and j are the state indices, and σ is the spin index. The Coulomb matrix K^C is defined as

$$K_{ij\sigma_1,kl\sigma_2}^C = (n_{ij\sigma_1} | n_{kl\sigma_2}) := \int \frac{d\mathbf{r}d\mathbf{r}'}{|\mathbf{r} - \mathbf{r}'|} n_{ij\sigma_1}^*(\mathbf{r}) n_{kl\sigma_2}(\mathbf{r}'), \quad (50)$$

where the orbital pair density is $n_{ij\sigma}(\mathbf{r}) = \psi_{i\sigma}^*(\mathbf{r})\psi_{j\sigma}(\mathbf{r})$.

When i, j both refer to valence states, the pair density can be partitioned into a smooth part and atom-centered corrections, similar to the AE density in Eq. (13), as

$$n_{ij\sigma} = \tilde{n}_{ij\sigma} + \sum_a (n_{ij\sigma}^a - \tilde{n}_{ij\sigma}^a). \quad (51)$$

Due to the non-local nature of the Coulomb kernel $1/|\mathbf{r} - \mathbf{r}'|$, direct insertion of Eq. (51) into Eq. (50) leads to cross terms between different augmentation spheres. The same problem appeared already in the evaluation of the PAW Coulomb energy, and it can be solved similarly by introducing compensation charges (from now on we drop the spin

indices for brevity)

$$\tilde{Z}_{ij}^a(\mathbf{r}) = \sum_{\ell m} Q_{\ell m, ij}^a \hat{g}_{\ell m}^a(\mathbf{r}), \quad (52)$$

which are chosen to electrostatically decouple the smooth compensated pair densities

$$\tilde{\rho}_{ij} = \tilde{n}_{ij} + \sum_a \tilde{Z}_{ij}^a. \quad (53)$$

The Coulomb matrix now has a simple partitioning in terms of a smooth part and local corrections,

$$K_{ij,kl}^C = (\tilde{\rho}_{ij} | \tilde{\rho}_{kl}) + \sum_a \Delta K_{ij,kl}^{C,a}. \quad (54)$$

We refer to Ref. [51] for the exact form of the correction term $\Delta K_{ij,kl}^{C,a}$, which is also used to evaluate Eq. (20). We note that the Coulomb matrix $K_{ij,kl}^C$ appears also in the linear-response TDDFT (see Sec. 5) and in the GW method [52].

The formally exact partitioning in Eq. (54) retains all information about the nodal structure of the AE wave functions in the core region, which is important due to the non-local probing of the Coulomb operator. In standard pseudopotential schemes this information is lost, leading to an uncontrolled approximation to $K_{ij,kl}^C$.

As a technical issue, we note that integration over the the Coulomb kernel $1/|\mathbf{r}-\mathbf{r}'|$ is done by solving the associated Poisson equation $\nabla^2 \tilde{v}_{ij} = -4\pi \tilde{\rho}_{ij}$, for the Coulomb potential. However, the compensated pair densities $\tilde{\rho}_{ij}$ have a non-zero total charge, which leads to an integrable singularity in periodic systems. For periodic systems, the problem is solved by subtracting a homogeneous background charge from the pair-densities and adding a correction term to the calculated potential afterwards [50, 53]. For non-periodic systems, the Poisson equation is solved by adjusting the boundary values according to the multipole expansion of the pair density.

Terms in the Coulomb matrix where either i or j refers to a core orbital can be reduced to trivial functions of the expansion coefficients P_{in}^a , Eq. (7). Although the valence-core interaction is computationally trivial to include, it is not unimportant, and we will return to the effect of neglecting it, as it is unavailable in pseudopotential schemes. The core-core exchange is simply a constant energy that can be calculated once and for all for every atom given the frozen core orbitals.

The Fock operator $v^F(\mathbf{r}, \mathbf{r}')$ corresponding to the exact-exchange energy functional of Eq. (49) is non-local, and it is difficult to represent on any realistic grid. Fortunately, in the iterative minimization schemes used in GPAW the explicit form is never needed, but it suffices to evaluate only the action of the operator on a wave function. By taking into account the PAW transformation, the action on the PS wave function can be derived by the relation.

$$f_n \hat{v}^F |\tilde{\psi}_n\rangle = \partial E_{xx} / \partial \langle \tilde{\psi}_n |, \quad (55)$$

which results in

$$f_n \hat{v}^F |\tilde{\psi}_n\rangle = - \sum_m f_m \tilde{v}_{nm}(\mathbf{r}) |\tilde{\psi}_m\rangle + \sum_a \sum_i |\tilde{p}_i^a\rangle \Delta v^{Fa} [\tilde{v}_{nm}, \{P_{jm}^a\}]. \quad (56)$$

The computationally demanding first term is related to smooth pseudo quantities only, which can be accurately represented on coarse grids, making it possible to do converged self-consistent EXX calculations at a relatively modest cost. Applying the Fock operator is, however, still expensive, as a Poisson equation must be solved for all pairs of orbitals. The atomic correction Δv^{Fa} depends both on \tilde{v}_{nm} and on the set of expansion coefficients P_{in}^a . The details of the derivation as well as the exact form of the correction term can be found in Ref. [54].

As a benchmark of the implementation, and for comparing the PBE and hybrid PBE0 [55] functionals, we have computed the atomization energies of the G2-1 database of molecules [56] using these two functionals. The results are compared to the experimental values as well as to the results of the planewave PAW implementation VASP, and of the all-electron atomic-orbital code Gaussian 03, as reported in Ref. [50].

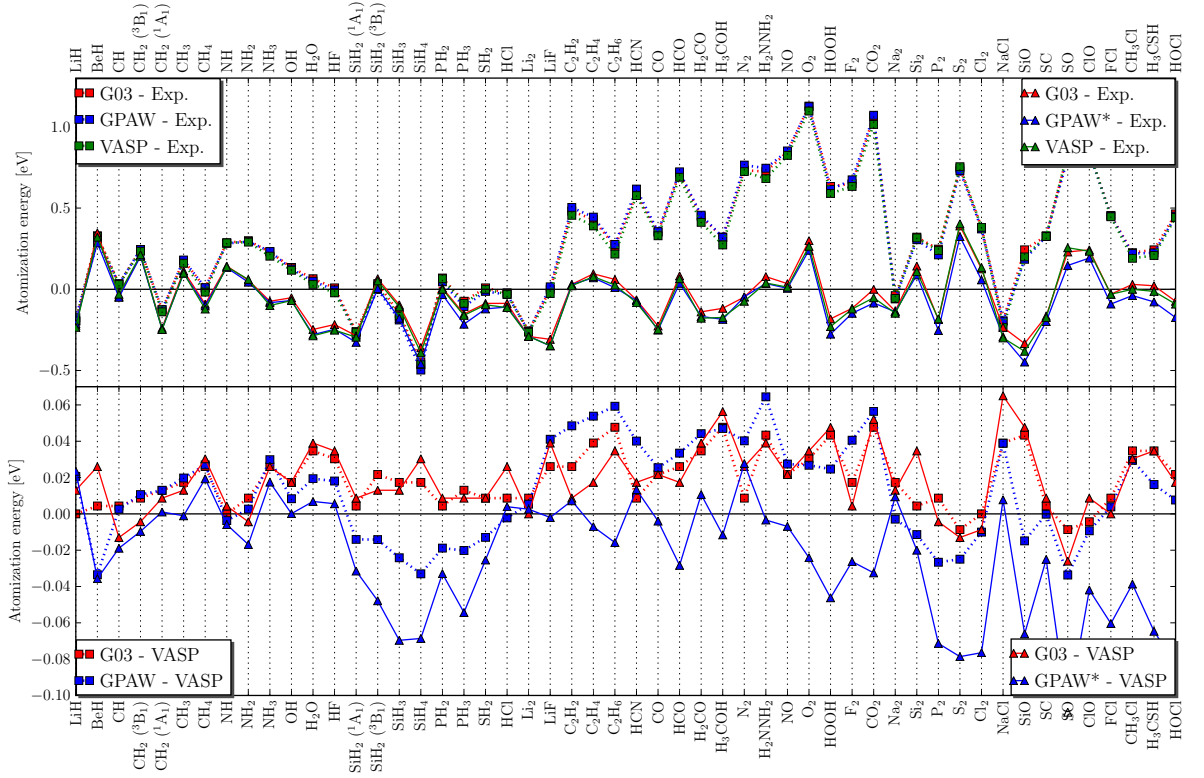


Figure 2: Calculated atomization energies using PBE (dotted) and PBE0 (solid) functionals compared to experimental values (top) and to VASP (bottom). GPAW PBE0 values are not geometry optimized (evaluated at PBE geometries)

The PBE0 functional includes a fraction (25%) of Fock exchange in PBE, which improves the agreement with experiments significantly, as shown in Fig. 2. The figure shows also that the different implementations deviate from one another by less than 0.05 eV on average. The GPAW PBE0 energies are all slightly too small because they have not been geometry optimized with the hybrid functional (they are evaluated at PBE geometries).

The importance of the valence-core exchange interaction for this test suite is typically a few tenths of eV for the atomization energy, but can induce a shift of several eV in the

eigenvalues of the frontier orbitals.

The difference in atomization energy between EXX evaluated using PBE orbitals and self-consistent EXX orbitals is less than 13 meV on average suggesting that PBE and HF orbitals are very similar. The difference in self-consistency is even less for PBE0. Also, for the eigenvalues of the EXX (or PBE0) Hamiltonian the use of PBE orbitals has a small effect, differences being less than 0.1 eV in the worst case (CO₂).

3.3 GLLB approximation for the exact exchange

One drawback of the EXX approach is that the evaluation of the Fock operator is computationally quite expensive. Thus, it would be desirable to have computationally inexpensive approximations to the exact exchange. One such approximation (GLLB) is provided in Ref. [57], where the exchange potential v_x is separated into a screening part v_S and a response part v_{resp} ,

$$v_x(\mathbf{r}) = v_S(\mathbf{r}) + v_{\text{resp}}(\mathbf{r}), \quad (57)$$

and the two parts are approximated independently.

In the original work v_S is approximated with the GGA exchange energy density ϵ_x^{GGA} of Becke [58]

$$v_S(\mathbf{r}) = \frac{2\epsilon_x^{GGA}(\mathbf{r}; n)}{n(\mathbf{r})}. \quad (58)$$

Using the common denominator approximation, exchange scaling relations and asymptotic behaviour, the response part is approximated as

$$v_{\text{resp}}(\mathbf{r}) = \sum_i^{\text{occ}} K[n] \sqrt{\varepsilon_r - \varepsilon_i} \frac{|\psi_i(\mathbf{r})|^2}{n(\mathbf{r})}, \quad (59)$$

where ε_r is the highest occupied eigenvalue. The coefficient $K[n]$ can be determined for the homogeneous electron gas, where it is a constant

$$K = \frac{8\sqrt{2}}{3\pi^2} \approx 0.382. \quad (60)$$

In addition to the above GLLB potential, we have implemented an extension (GLLB-SC) which contains also correlation and is targeted more to solids [59]. Instead of the exchange potential, the whole exchange-correlation potential $v_{xc}(\mathbf{r})$ is separated into two parts. The screening part is approximated now with the PBEsol [60] exchange-correlation energy density and the response part contains also contribution from the PBEsol response potential,

$$v_{\text{resp}}(\mathbf{r}) = \sum_i^{\text{occ}} K \sqrt{\varepsilon_r - \varepsilon_i} \frac{|\psi_i(\mathbf{r})|^2}{n(\mathbf{r})} + v_{\text{resp}}^{\text{PBEsol}}(\mathbf{r}). \quad (61)$$

An important property of the exact exchange-correlation potential is the discontinuity at integer occupation numbers N ,

$$\Delta_{xc} = \lim_{\delta \rightarrow 0} [v_{xc}(\mathbf{r}; N + \delta) - v_{xc}(\mathbf{r}; N - \delta)]. \quad (62)$$

The derivative discontinuity is especially important for the band gaps of semiconductors and insulators, as the true quasiparticle band gap E_g^{QP} is a sum of the Kohn-Sham band gap E_g^{KS} and the discontinuity [61, 62]

$$E_g^{QP} = E_g^{KS} + \Delta_{xc}. \quad (63)$$

Neither LDA nor GGA potentials exhibit the discontinuity, which explains partly their failure in reproducing experimental band gaps. On the other hand, in the GLLB and GLLB-SC approximations one obtains an estimate for the discontinuity. As a result, GLLB-SC gives good description for the band gap of several materials as shown in Table. 1.

Table 1: The minimum Kohn-Sham bands gaps for LDA and GLLB-SC together with derivative discontinuity and the quasiparticle band gap of GLLB-SC. Experimental values are from Ref. [63]. All values are in eV.

Material	E_g^{KS} (LDA)	E_g^{KS}	Δ_{xc}	E_g^{QP}	exp.
C	4.09	4.14	1.27	5.41	5.48
Si	0.443	0.68	0.32	1.00	1.17
GaAs	0.36	0.79	0.25	1.04	1.63
AlAs	1.34	1.67	0.82	2.49	2.32
LiF	8.775	10.87	4.09	14.96	14.2
Ar	8.18	10.28	4.69	14.97	14.2

3.4 van der Waals functional

Van der Waals interactions are due to long range correlation effects that are not included in GGA-type XC functionals. The recently developed functional which includes van der Waals interactions [64] (vdW-DF) is available in GPAW.

The vdW-DF is a sum of a GGA exchange and a correlation term consisting of both short-ranged correlation (evaluated in the local density approximation) and longer-ranged correlation (depending nonlocally on the electron density) [65]:

$$E_c^{nl}[n] = \frac{1}{2} \int d\mathbf{r}_1 d\mathbf{r}_2 n(\mathbf{r}) \phi(q_1 r_{12}, q_2 r_{12}) n(\mathbf{r}_2), \quad (64)$$

where $\phi(d_1, d_2)$ is the vdW-DF kernel, $r_{12} = |\mathbf{r}_1 - \mathbf{r}_2|$ and q_1 and q_2 are the values of a universal function $q_0(n(\mathbf{r}), |\nabla n(\mathbf{r})|)$ evaluated at the two points \mathbf{r}_1 and \mathbf{r}_2 . Instead of n , we use the PS valence density \tilde{n} for the evaluation of Eq. (64). The justification for this choice is that $q_0(\mathbf{r})$ has very high values close to the nuclei, and the vdW kernel $\phi(d_1, d_2)$ in terms of the rescaled distances $d_1 = q_1 r_{12}$ and $d_2 = q_2 r_{12}$ will be quite short ranged and therefore not important for studying interactions between atoms.

Evaluation of $E_c^{nl}[\tilde{n}]$ by direct summation in real-space has an operation count that scales as N_g^2 (N_g is the number of grid points), which is often too time consuming for typical

calculations. We have therefore implemented the fast Fourier transformation (FFT) technique introduced by Román-Pérez and Soler [66] where the scaling is $N_g \log N_g$. As an example, a self-consistent vdW-DF calculation for water (64 molecules on 16 processors) takes only 80 % longer than a self-consistent PBE calculation. Additional details of our implementation can be found in Ref. [67].

3.4.1 DFT+U

In strongly correlated materials such as transition metal oxides, lanthanides or actinides the strong on-site Coulomb interaction of the localized d or f electrons is not correctly described by LDA or GGA. The basic idea behind the DFT+U method is to treat this interaction with an additional Hubbard-like term. The strength of the on-site interactions are usually described by semi-empirical parameters U and J . The GPAW implementation is based on the particular branch of DFT+U suggested in Ref. [68] where only a single effective $U_{\text{eff}} = U - J$ accounts for the Coulomb interaction, neglecting thereby any higher multi-polar terms.

Following Ref. [68], the DFT+U total energy is

$$E_{\text{DFT+U}} = E_{\text{DFT}} + \sum_a \frac{U_{\text{eff}}}{2} \text{Tr}(\rho^a - \rho^a \rho^a), \quad (65)$$

where ρ^a is the atomic orbital occupation matrix (AOOM).

In order to evaluate Eq. (65), a mapping between the wave functions and AOOM $\rho_{mm'}^a$ is required. This mapping can be written in terms of the density matrices $D_{n\ell m, n'\ell m'}^a$, Eq. (10), and the AE atomic orbitals $\phi_{n\ell m}^a$ as [69]

$$\rho_{mm'}^a = \sum_{n, n'} D_{n\ell m, n'\ell m'}^a \langle \phi_{n\ell m}^a | \phi_{n'\ell m'}^a \rangle.$$

The orbital quantum number ℓ is restricted to the orbital of interest and m restricted to the associated magnetic quantum numbers. The n index refers to the n th projector of the particular ℓ -channel. GPAW atomic setups have typically $n \in (1, 2)$ where $n = 1$ is the bound-state projector and $n = 2$ is unbound-state projector. Because of the latter, we truncate the integration in $\langle \phi_{n\ell m}^a | \phi_{n'\ell m'}^a \rangle$ at the augmentation sphere radius. The DFT+U energy correction adds also a term to the Hamiltonian within the augmentation spheres, $\Delta H_{i_1 i_2}^a$ in Eq. (31), which is obtained by taking the derivative of Eq. (65) with respect to $D_{i_1 i_2}^a$.

As an example, we show in Fig. 3 the calculated spin-magnetic-moment μ and the fundamental band gap Δ_g of CoO and NiO with increasing values of the effective Hubbard U_{eff} . The figure shows clearly that the DFT+U scheme improves the description of the strongly correlated nature of the transition metal oxide. The calculations have been carried out using the PBE exchange-correlation functional, a grid spacing of 0.16 Å and 8x8x8 k-points in the Brillouin zone. In all calculations, the lattice constants are optimized with pure PBE ($U_{\text{eff}} = 0$) with a grid spacing of 0.16 Å, the obtained values are 4.19 Å for

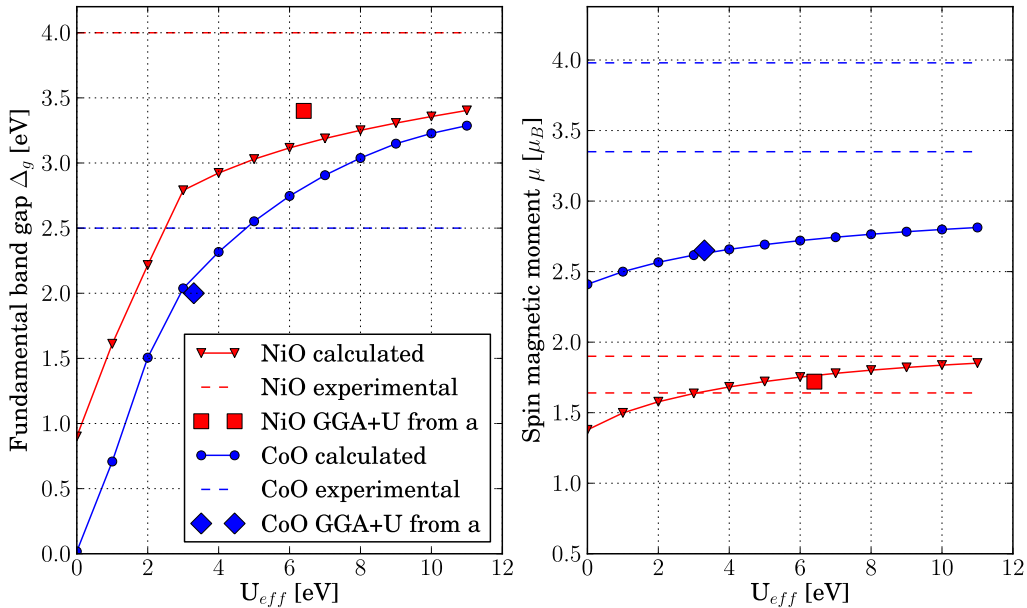


Figure 3: Fundamental band gap Δ_g (left) and the spin magnetic moment μ (right), for the AFMII phase of NiO and CoO as a function of the applied Hubbard U_{eff} . a: L. Wang *et. al.* [70]. Experimental values are as cited in Ref. [71]. Two different experimental values are shown for the spin magnetic moment.

NiO and 4.24\AA for CoO. The corresponding experimental values are 4.17\AA and 4.25\AA for NiO and CoO, respectively.

4 Error estimation

Density-functional theory is used extensively to calculate binding energies of different atomic structures ranging from small molecules to extended condensed-matter systems. A number of different approximations to the exchange-correlation energy have been developed with different scopes in mind and with different virtues. When it comes to the practical use of DFT it is therefore usually very much up to the user to obtain experience with the different xc-functionals and gain insight into how accurate the calculations are for a particular application. This learning process can be rather slow and also for other more general reasons it would be advantageous to have a reliable and unbiased way to estimate errors on DFT calculations.

The error estimation implemented in GPAW is inspired by ideas from Bayesian statistics [72]. The ingredients in a typical statistical model construction consist of 1) a database with a number of (possibly noisy) data points which the model is supposed to reproduce as closely as possible and 2) the model which is described by a number of parameters which can be adjusted to improve the model. The quality of the model can for example be estimated by a least-squares cost which is a sum over all data points of the squared difference between the database value and the value predicted by the model. The cost

thus becomes a function of the model parameters and minimization of the cost leads to the best-fit model. (An important issue here is to control the effective number of parameters in the model to avoid over-fitting, but we shall not go into this here). So far we have described a common least-squares fit. What the Bayesian approach adds to this is the idea of not only a single best-fit model but an ensemble of models representing a probability distribution in model space. Using the ensemble, the model no longer predicts only a single value for a data point but a distribution of values which will be more or less scattered depending on the ability of the model to make an accurate prediction for that point.

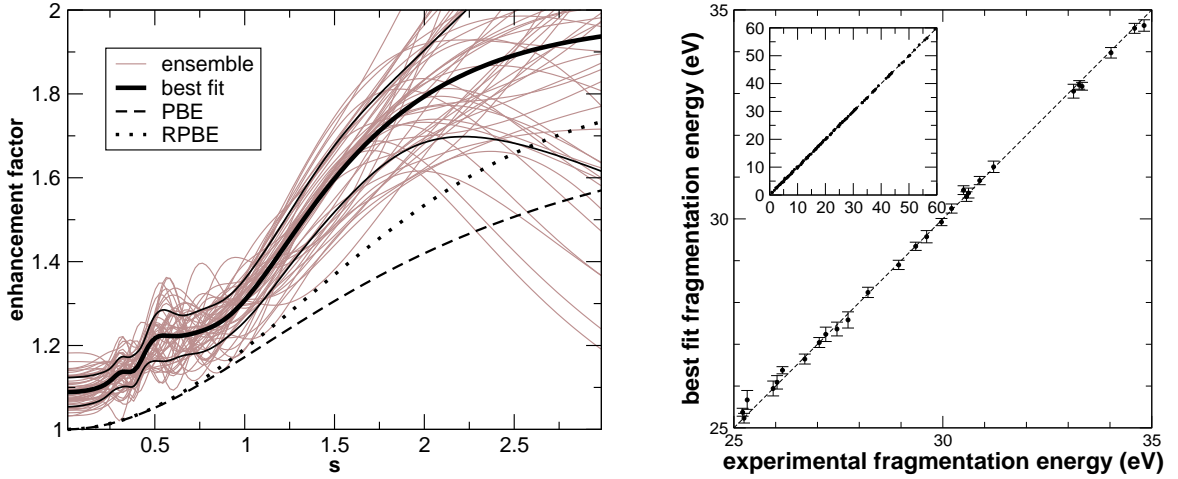


Figure 4: Left: Ensemble of enhancement factors as optimized to the experimental fragmentation energies of 148 molecules. The thin black lines running parallel to the best fit mark the width of the ensemble. The PBE and RPBE enhancement factors are also shown for comparison, s is the reduced density gradient. Right: Fragmentation energies predicted with the best fit enhancement factor versus the experimental values. The error bars are calculated from the ensemble in the left panel.

In the case of GPAW, we have worked on providing error estimates for GGA-type calculations. The model space is defined by a suitable parametrization of the exchange enhancement factor f_x , which enters the exchange functional as (see Ref. [73] for details)

$$E_x[n] = \int f_x(s(\mathbf{r}); \theta) n(\mathbf{r}) \varepsilon_x^{\text{unif}}(n(\mathbf{r})) d\mathbf{r}.$$

Here, s is the reduced density gradient $\sim |\nabla n|/n$, and θ our parametrization. The database consists of the experimental fragmentation energies of 148 small molecules (from the G2 neutral test set [56]). The left panel in Fig. 4 displays the resulting Bayesian ensemble of enhancement factors in terms of some randomly drawn members. The enhancement factor for the best-fit model is seen to resemble other commonly used enhancement factors like PBE, and RPBE. It should be noted that for a typical Bayesian ensemble the spread is governed mostly by the noise in the data points and the limitations in the number of data points. In our case the noise in the experimental fragmentation energies is quite small compared with a typical deviation between the experimental value and the best-fit

value. This is an indication that our model space is incomplete, i.e. there is simply a limit to how accurate a GGA-type functional can be. The width of the ensemble shown in Fig. 4 is therefore controlled not so much by the noise as by the model incompleteness. The ensemble can be used to estimate errors as also shown in Fig. 4. Here the calculated fragmentation energies for the molecular database are shown together with the estimated error bars versus the experimental values. The average of the predicted error bars squared reproduces by construction of the ensemble the average value of the squared deviation between experiment and best-fit model. The detailed transferability of the best-fit model and the error predictions to other classes of systems is currently under investigation.

5 Time-dependent density-functional theory

Standard DFT is applicable only to the ground state properties of a system. However, there are many properties of great interest which are related to the excited states, e.g. optical absorption spectrum. Time-dependent density-functional theory (TDDFT) [3] is the extension of standard DFT into the time-domain enabling the study of excited state properties. There are two widely used formulations of TDDFT, the real-time propagation scheme [74] and the linear-response scheme [75]; both of these are available in GPAW. The details of the implementations are described in Ref. [51], and we present only a brief overview here.

5.1 Real-time propagation

The time-dependent AE Kohn-Sham equation is

$$i\frac{\partial}{\partial t}\psi_n(t) = \hat{H}(t)\psi_n(t), \quad (66)$$

where the time-dependent Hamiltonian $\hat{H}(t)$ can include also an external time-dependent potential. Assuming that the overlap matrix \hat{S} is independent of time, this equation can be written in the PAW formalism as

$$i\hat{S}\frac{\partial}{\partial t}\tilde{\psi}_n(t) = \hat{H}(t)\tilde{\psi}_n(t). \quad (67)$$

This time-dependent equation can be solved using the Crank-Nicolson propagator with a predictor-corrector step as described in Ref. [51].

5.2 Linear-response formalism

Within the linear-response regime, the excitation energies can be calculated from the eigenvalue equation of the form

$$\mathbf{\Omega}F_I = \omega_I^2 F_I, \quad (68)$$

where ω_I is the transition energy from the ground state to the excited state I and F_I denotes the associated eigenvector. The matrix $\mathbf{\Omega}$ can be expanded in Kohn-Sham single

particle-hole excitations leading to

$$\Omega_{ij\sigma,kl\tau} = \delta_{ik}\delta_{jl}\delta_{\sigma\tau}\varepsilon_{ij\sigma}^2 + 2\sqrt{f_{ij\sigma}\varepsilon_{ij\sigma}f_{kl\tau}\varepsilon_{kl\tau}}K_{ij\sigma,kl\tau}, \quad (69)$$

where $\varepsilon_{ij\sigma} = \varepsilon_{j\sigma} - \varepsilon_{i\sigma}$ are the energy differences and $f_{ij\sigma} = f_{i\sigma} - f_{j\sigma}$ are the occupation number differences of the Kohn-Sham states. The indices i, j, k, l are state indices, whereas σ, τ denote spin indices. The coupling matrix can be split into two parts $K_{ij\sigma,kl\tau} = K_{ij\sigma,kl\tau}^C + K_{ij\sigma,kl\tau}^{xc}$. The former Coulomb matrix has exactly the same form as in the context of exact exchange, Eq. (50)

$$K_{ij\sigma,kl\tau}^C = (n_{ij\sigma}|n_{kl\tau}) \quad (70)$$

and is often called the random phase approximation part. It describes the effect of the linear density response via the classical Hartree energy. The second contribution is the exchange-correlation part

$$K_{ij\sigma,kq\tau}^{xc} = \int d\mathbf{r}_1 d\mathbf{r}_2 n_{ij\sigma}^*(\mathbf{r}_1) \frac{\delta^2 E_{xc}}{\delta n_{\sigma}(\mathbf{r}_1) \delta n_{\tau}(\mathbf{r}_2)} n_{kq\tau}(\mathbf{r}_2), \quad (71)$$

where n_{σ} is the spin density. The functional derivative can be calculated with a finite difference scheme.

Diagonalization of the linear-response equation (68) gives directly all the excitation energies in the linear-response regime. As an example, Table 2 shows the calculated excitation energies of a CO molecule together with reference calculations. The agreement between our results and numerically accurate AE results [76] is generally good.

Table 2: Calculated excitation energies of CO molecule within the LDA approximation in eV. Bond length is 1.128 Å

State	Spin	GPAW	AE [76]
a $^3\Pi$	triplet	5.95	6.03
A $^1\Pi$	singlet	8.36	8.44
a' $^3\Sigma^+$	triplet	8.58	8.57
b $^3\Sigma^+$	triplet	9.01	9.02
B $^1\Sigma^+$	singlet	9.24	9.20
d $^3\Delta$	triplet	9.25	9.23
I $^1\Sigma^-$	singlet	9.87	9.87
e $^3\Sigma^-$	triplet	9.87	9.87
D $^1\Delta$	triplet	10.35	10.36

Within the time-propagation scheme, one obtains only the excitations corresponding to a particular initial perturbation. Thus, different types of perturbations would be needed to reach different excited states. In the case of a singlet ground state molecule like CO, the often applied delta pulse perturbation (as introduced in the following section) can lead only to dipole allowed singlet-singlet excitations. Therefore the triplet excitations

and dipole forbidden singlet excitation at 9.87 eV do not appear in the time-propagation scheme.

5.3 Optical absorption spectra

In the real-time formalism the linear absorption spectrum can be obtained by exciting the system first with a weak delta pulse,

$$\mathbf{E}(t) = \epsilon \mathbf{k}^{\circ} \delta(t), \quad (72)$$

where ϵ is a unitless perturbation strength parameter and \mathbf{k}° is a unit vector giving the polarization direction of the field. The delta pulse changes the initial wave functions to

$$\psi(t = 0^+) = \exp\left(i \frac{\epsilon}{a_0} \mathbf{k}^{\circ} \cdot \mathbf{r}\right) \psi(t = 0^-). \quad (73)$$

The system is then let to evolve freely and during the time-evolution the time-dependent dipole moment $\boldsymbol{\mu}(t)$ is recorded. At the end of the calculation, the dipole strength tensor and oscillator strengths are obtained via a Fourier transform.

In the linear-response formalism one needs also the eigenvectors of Eq. (68) when calculating the absorption spectrum. Together with the Kohn-Sham transition dipoles

$$\boldsymbol{\mu}_{ij\sigma} = \langle \psi_{i\sigma} | \mathbf{r} | \psi_{j\sigma} \rangle \quad (74)$$

the oscillator strengths are given by

$$f_{I\alpha} = \left| \sum_{ij\sigma}^{f_{i\sigma} > f_{j\sigma}} (\boldsymbol{\mu}_{ij\sigma})_{\alpha} \sqrt{f_{ij\sigma} \epsilon_{ij\sigma}} (F_I)_{ij\sigma} \right|^2. \quad (75)$$

The discrete oscillator strengths can be folded by a gaussian (as an example) for comparison with the time-propagation calculation and experiments

Fig. 5 shows the calculated linear absorption spectra of a CH₄ molecule. The agreement between the completely different numerical schemes is remarkable.

Even though the time-propagation scheme is relatively time-consuming in small systems, the favourable scaling with system size as well as the good parallelization possibilities (described in more detail in Sec. 8) enable calculations also for large systems. As an example, Fig. 6 shows the calculated optical spectra of Au₂₅(S-CH₃)₁₈⁻, Au₂₅(S-CH₂-CH₂-C₆H₅)₁₈⁻, and Au₁₀₂(S-CH₃)₄₄. The shapes of Au₂₅(SR)₁₈⁻ spectra are similar to experimental spectra in Ref. [77]. However, all features appear systematically at too low energy. This is most probably due to ALDA approximation. The Au₁₀₂(S-CH₃)₄₄ spectrum has less structure than the smaller clusters and it also shows a significant red shift of 0.6 eV.

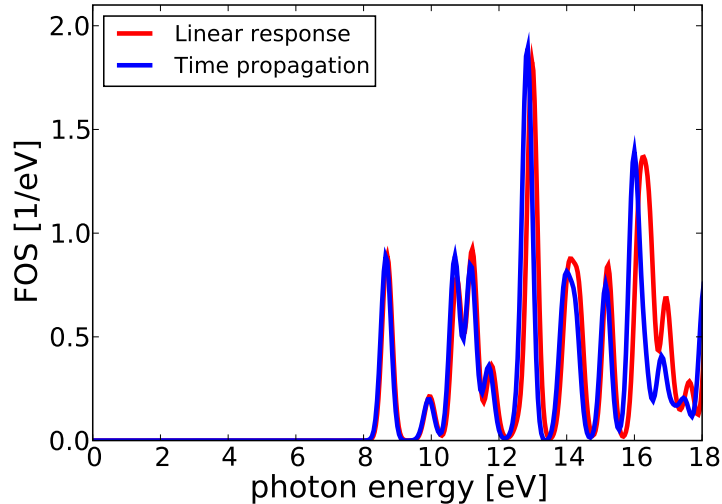


Figure 5: Calculated optical absorption spectra of CH_4 molecule presented as folded oscillator strengths (FOS). The calculation is performed both with the time-propagation and the linear-response method.

5.4 Non-linear emission spectra

The time-propagation approach can be used also in the non-linear regime where the linear-response scheme is no longer applicable. For example, a strong laser field can introduce non-linear terms in the polarizability of an atom or molecule. Fig. 7 shows the emission spectra of Mg atom in laser field with frequency 0.5 eV and strength 0.01 and 0.05 atomic units. Due to non-linear effects, harmonics of the laser field frequency appear at the odd integer multiples of the driving field. The intensity depends nonlinearly on the strength of the field. The harmonics at even integer multiples are forbidden by the symmetry. In the simulated spectrum, weak even harmonics are observed due to numerical inaccuracies. Compared to our earlier calculation with beryllium [51], the Mg spectra has less numerical noise, which is because of the imaginary potential absorbing boundary conditions [78] used in the calculation of Mg spectra.

5.5 Photoelectron spectra

The process of photoionization may be viewed in two different ways. In the simplest interpretation, the single-particle states of Kohn-Sham DFT are directly connected to the observed electrons in the experiment. Even though the orbital energies (except for the highest occupied orbital) do not have rigorous physical meaning, they often give a very reasonable description of the experimentally observed electron binding energies E_{bind} [79]. A more rigorous description of the photoelectron spectrum (PES) is available in the many-body picture. The “daughter” system, after emitting the electron, is left either in the electronic ground state or in an electronically excited state when the released electron

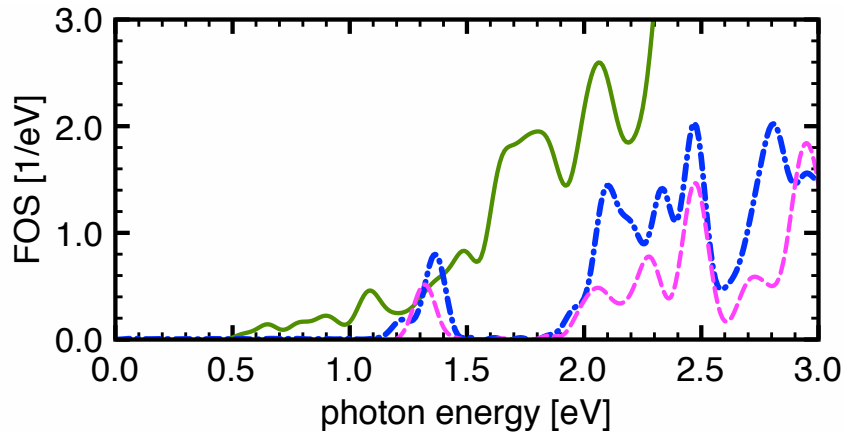


Figure 6: Optical absorption spectra of $\text{Au}_{25}(\text{S-CH}_3)_{18}^-$ (dashed magenta), $\text{Au}_{25}(\text{S-CH}_2\text{-CH}_2\text{-C}_6\text{H}_5)_{18}^-$ (dash-dotted blue), and $\text{Au}_{102}(\text{S-CH}_3)_{44}$ (solid green).

has reached the detector. The measured kinetic energy distribution of the ejected electron is given by the difference between the ground state energy of the “mother” system E_0^N and excited state energies of the daughter system E_I^{N-1}

$$E_{\text{bind}} = E_I^{N-1} - E_0^N, \quad (76)$$

where N denotes the number of electrons. The ground state energy and excitation energies can be calculated with DFT and TDDFT, respectively. However, it is not only the energies that determine the amount of electrons in the detector, but also the probability for ionization, i.e. not all excited states of the daughter system can be reached by ionizing the mother system.

In principle, one would need the many-particle wave-functions to be able to calculate the transition probabilities, but these are not available in DFT. One can nevertheless create an approximate scheme to calculate the overlaps [80]: The ground state wave functions of daughter and mother systems are approximated by a single Slater determinant of the occupied Kohn-Sham orbitals. The excited-state wave functions of the daughter states are constructed via the weights F_I (eq. 68) of the Kohn-Sham single orbital excitations. With these approximations one can evaluate the spectroscopic factor f_I , the energy independent probability for the daughter system to end up in a given excited state I due to photoemission.

We have implemented this scheme in GPAW. As an example, we have calculated the resultant PES spectrum of H_2O , CO and NH_3 . Figure 8 shows the comparison of the spectroscopic factors with experiments and the single particle Kohn-Sham approach, where the spectroscopic factor is unity for each occupied orbital. Both the Kohn-Sham approach and the linear-response TDDFT scheme give good agreement with experiment for lower bound electrons. For peaks at high binding energies, there is a clear improvement by the new scheme. In particular the “broadening” of the highest energy peak can not be described by the Kohn-Sham single particle picture. Here many excitations of the daughter

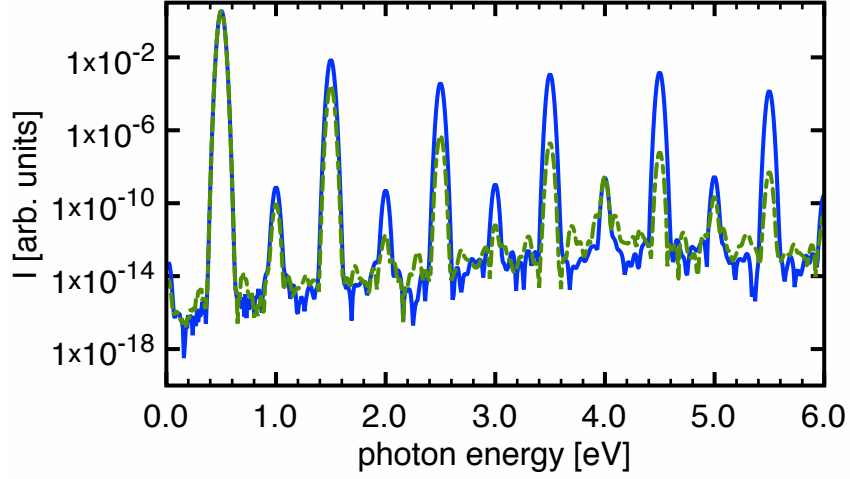


Figure 7: Non-linear emission spectra of Mg atom in a laser field of frequency 0.5 eV and strength of 0.01 (solid blue) and 0.05 (dashed green) atomic units. Strong harmonic frequency generation is observed at odd multiples of the laser field frequency.

system contribute to the peak.

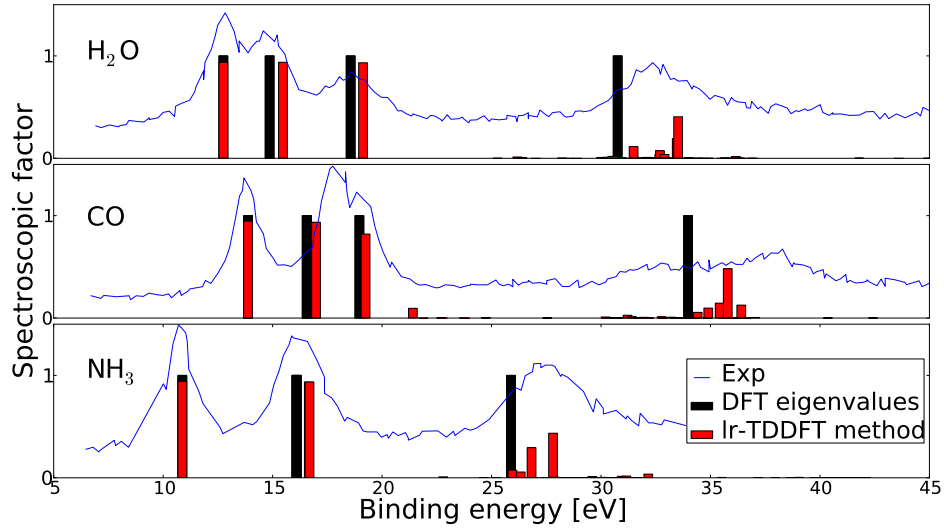


Figure 8: Experimental photoelectron cross sections (adapted from ref. [81]) compared with spectroscopic factors from TDDFT and Kohn-Sham approaches.

6 Localized atomic-like basis functions

As an alternative to the grid-based finite-difference approach described above, GPAW offers also the possibility to work with atomic-like basis functions, or linear combinations of atomic orbitals (LCAO). A detailed description of GPAW's LCAO implementation is available in Ref. [82]. An LCAO basis function centered at atom a has the form

$$\Phi_{nlm}^a(\mathbf{r}) = R_{nl}^a(|\mathbf{r} - \mathbf{R}^a|)Y_{lm}(\mathbf{r} - \mathbf{R}^a), \quad (77)$$

where $R_{n\ell}^a$ is a radial function which vanishes beyond a certain cut-off radius, and $Y_{\ell m}$ is a spherical harmonic. By defining ν as the composite a, n, ℓ, m , a general PAW state i can then be expanded as

$$\tilde{\psi}_i = \sum_{\nu} C_{i\nu} \Phi_{\nu}(\mathbf{r}), \quad (78)$$

where $C_{i\nu}$ are expansion coefficients.

The grid method and the localized basis complement each other very well. With the grid-based scheme the complete basis set limit can be systematically reached while the localized basis allows for fast calculations in situations where efficiency is more important than high accuracy. Moreover, the localized basis is well suited for quantum transport calculations, linear-scaling computation schemes, molecular dynamics simulations, as well as for analysis purposes. The "multi-basis" feature of GPAW allows the user to switch seamlessly between the accurate grid mode and the efficient LCAO mode at any point of a computation. For example, the first part of a structural optimization could be performed efficiently using the minimal localized basis while the final steps could be performed in the "grid mode". To our knowledge GPAW is the first code combining localized basis functions with the PAW method, *and* the first code supporting two different representations for the Kohn-Sham orbitals within the same unifying DFT framework, that is, with exactly the same set of approximations.

The LCAO implementation reuses most of what is implemented in the finite-difference PAW method: calculation of electrostatic interactions, evaluation of the XC potential, atomic PAW energy-corrections, density mixing and also most of the contributions to the atomic forces are the same. It is only the evaluation of overlap integrals and matrix elements of the kinetic energy operator that are done differently. Instead of calculating integrals like $\langle \tilde{\psi}_n | \hat{S} | \tilde{\psi}_m \rangle$, $\langle \tilde{\psi}_n | \hat{T} | \tilde{\psi}_m \rangle$, and $\langle \tilde{p}_i^a | \tilde{\psi}_n \rangle$ on a 3-d grid and using a finite-difference representation for \hat{T} , we express these integrals in terms of two-center integrals of the type: $\langle \Phi_{\mu} | \Phi_{\nu} \rangle$, $\langle \Phi_{\mu} | \hat{T} | \Phi_{\nu} \rangle$, and $\langle \tilde{p}_i^a | \Phi_{\nu} \rangle$, where Φ_{μ} are the atomic-like basis functions. These integrals can be pre-calculated as described in Ref. [11].

Because of the much smaller number of degrees of freedom in a LCAO calculation compared to a grid-based calculation, we can do a complete diagonalization in the subspace of our basis set instead of being forced to use iterative diagonalization techniques.

A minimal atomic basis set consists of one modified atomic orbital for each valence state – the single-zeta basis functions. First, localized atomic-like orbitals Φ^{AE} are obtained for each valence state by solving the radial AE Kohn-Sham equations for the isolated atom. In order to ensure that the wave function vanishes beyond a certain cutoff radius, the atom is placed in a suitably defined confining potential well [83]. The basis functions are then obtained using $\Phi(\mathbf{r}) = \mathcal{T}^{-1} \Phi^{\text{AE}}(\mathbf{r})$. The cutoff radius is selected in a systematic way by specifying the energy shift ΔE of the confined orbital compared to the free-atom orbital [84]. In this approach small values of ΔE will correspond to long-ranged basis orbitals [82].

In order to improve the radial flexibility, extra basis functions with the same angular

momentum ℓ (multiple-zeta) are constructed for each valence state using the split-valence technique [11]. The extra function is constructed by matching a polynomial to the tail of the atomic orbital, where the matching radius is determined by requiring the norm of the part of the atomic orbital outside that radius to have a certain value.

Finally, polarization functions (basis functions with ℓ quantum number corresponding to the lowest unoccupied angular momentum) can be added in order to improve the angular flexibility of the basis. There are several approaches for generating these orbitals, such as perturbing the occupied eigenstate with the highest ℓ quantum number with an electric field using first order perturbation theory or using the appropriate unoccupied orbitals. In GPAW we use a Gaussian-like function of the form $r^\ell \exp(-\alpha r^2)$ for the radial part, where ℓ corresponds to the lowest unoccupied angular momentum.

One of the most time consuming parts of a basis set calculation is the evaluation of matrix elements of the effective pseudo-potential $\langle \Phi_\mu | \tilde{v} | \Phi_\nu \rangle$, which is done on a 3-d grid. For an efficient evaluation of these matrix elements, it is important to have as short-ranged basis functions as possible and to use as coarse grids as possible. For the latter, the PAW method helps to make the basis functions and potentials smooth.

Table 3: Lattice constants, a , cohesive energies, E_c , and bulk moduli, B , for selected solids. MAE denotes the mean absolute error of the double-zeta polarized (DZP) basis set with respect to the grid based results.

	a (Å)		E_c (eV)		B (GPa)	
	DZP	GRID	DZP	GRID	DZP	GRID
LiF	4.10	4.06	4.52	4.24	70	80
C	3.58	3.57	7.89	7.72	422	433
Na	4.24	4.19	1.07	1.09	7.9	7.9
MgO	4.27	4.26	4.97	4.95	173	154
Al	4.07	4.04	3.54	3.43	79	77
NaCl	5.67	5.69	3.26	3.10	26	24
Li	3.43	3.43	1.63	1.62	16.3	14.2
SiC	4.41	4.39	6.48	6.38	202	211
Si	5.49	5.48	4.71	4.55	86	88
AlP	5.53	5.51	4.21	4.08	81	82
Fe	2.83	2.84	5.07	4.85	231	198
Cu	3.64	3.65	4.14	3.51	143	141
Pt	3.98	3.98	5.69	5.35	263	266
MAE	0.019	0.0	0.18	0.0	7.4	0.0

As an example, Table 3 shows the lattice constant, cohesive energy, and bulk modulus for a range of solids calculated with double-zeta polarized (DZP) basis sets and compared to the grid based results. The cutoff radii of the basis orbitals correspond to an energy shift of 0.1 eV. The DZP values are in good agreement with the grid based values, in particular for the structural properties, i.e. lattice constants and bulk moduli. Cohesive energies

are more difficult to describe with a localized basis set. The primary source of error in cohesive energies comes from the free-atom calculation, where the confinement of each orbital raises the energy levels by around 0.1 eV. Thus, atomic energies are systematically overestimated, leading to stronger binding

6.1 Non-equilibrium electron transport

Driven by the prospects of nano-scale electronics, the field of quantum transport has developed rapidly over the last decade. In support of this development, GPAW supports open- boundary finite-bias electron transport calculations with the LCAO basis. The basic setting is that of a central device region (C) connected to two semi-infinite leads (L) and (R). The leads are kept at fixed chemical potentials, μ_L and μ_R , to simulate an applied bias voltage of $V = (\mu_L - \mu_R)/e$ across the device region. Due to electronic screening the electron potential inside the leads converges rapidly to the bulk value and this defines the boundary conditions for the electrostatic potential inside C. Rather than obtaining the wave functions from the eigenvalue equation we work with the Green function (GF) of the central region defined by

$$G(z) = (zS - H_C - \Sigma_L(z) - \Sigma_R(z))^{-1}, \quad (79)$$

where S and H_C are, respectively, the overlap and Kohn-Sham Hamiltonian matrix of the central region in the LCAO basis. The self-energies, $\Sigma_{L/R}$, represent the coupling to the leads and are obtained using the efficient decimation technique [85]. The electron density matrix is given by

$$D = \frac{1}{2\pi i} \int_{-\infty}^{\infty} G^<(\varepsilon) d\varepsilon = \frac{1}{2\pi i} \int_C G^<(z) dz \quad (80)$$

with the lesser GF defined by

$$G^<(z) = G(z)(\Sigma_L^<(z) + \Sigma_R^<(z))G(z)^\dagger \quad (81)$$

As indicated in the last equality of Eq. (80) the integral is performed along a complex contour C . The equivalence of the two expressions follows from the analytical properties of the Green function and residue calculus [86]. Away from the real axis the Green function varies slowly with z and the integral can be efficiently evaluated using a Gauss-Kronrod quadrature [87]. The non-equilibrium density is obtained from

$$\tilde{n}(\mathbf{r}) = \sum_{\nu\mu} D_{\nu\mu} \Phi_\nu(\mathbf{r})^* \Phi_\mu(\mathbf{r}) + \sum_a \tilde{n}_c^a, \quad (82)$$

where Φ_ν and Φ_μ are the LCAO orbitals in the central region and $D_{\nu\mu}$ are the corresponding matrix elements of the density matrix. The Poisson equation is solved on the real space grid to obtain the electrostatic contribution to the effective potential \tilde{v} in region C. The boundary conditions for the Poisson equation at the C-L and C-R interfaces are given by bulk potential of the leads (shifted by the applied bias voltage $\pm eV/2$), while periodic boundary conditions are used in the plane perpendicular to the direction of transport.

The cycle $D \rightarrow \tilde{n}(\mathbf{r}) \rightarrow \tilde{v}(\mathbf{r}) \rightarrow H_C \rightarrow D$ is iterated until self-consistency using Pulay density mixing. At self-consistency the current of a spin-degenerate system can be calculated from [88, 89]

$$I(V) = \frac{1}{\pi} \int_{-\infty}^{\infty} (f_L(\varepsilon) - f_R(\varepsilon)) \text{Tr}[\Gamma_L(\varepsilon)G(\varepsilon^+)\Gamma_R(\varepsilon)G(\varepsilon^+)^\dagger] d\varepsilon, \quad (83)$$

where $\varepsilon^+ = \varepsilon + i0^+$ and $\Gamma_{L/R}(\varepsilon) = i(\Sigma_{L/R}(\varepsilon^+) - \Sigma_{L/R}(\varepsilon^+)^\dagger)$ and the trace is taken over the central region basis functions.

As an example, Fig. 9 shows the IV curve of a molecular junction consisting of a benzene dithiol molecule attached to gold electrodes (see inset). We have used a DZP basis set for the molecule and SZ basis for the Au, a total of 84 Au atoms in the central region, and 4×4 k -points in the surface plane (8 irreducible). A 2-d plot of the average effective potential at a bias of 3 V is shown in the right panel. Although four Au layers are included in the central region on both sides of the molecule, electronic screening limits the potential drop to the molecule and outermost Au surface layer.

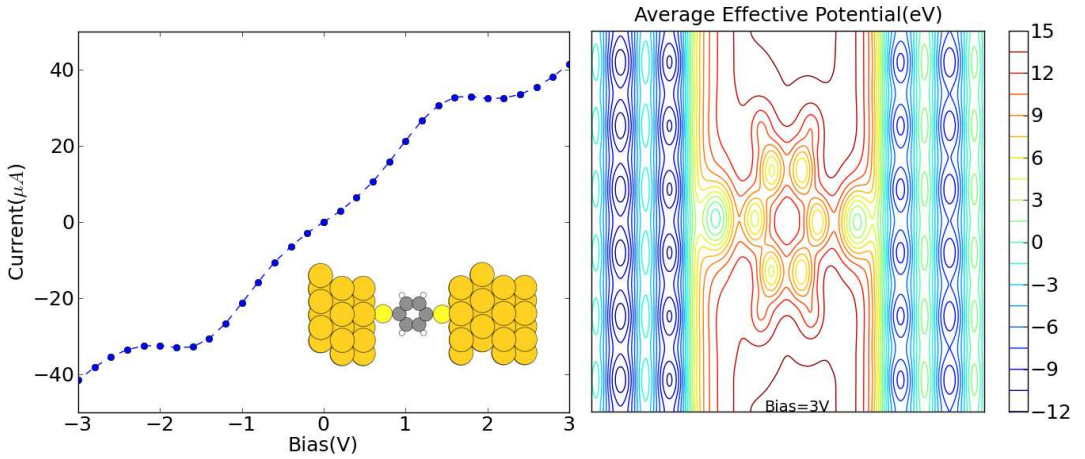


Figure 9: Left: Calculated IV curve for the Au/benzene-dithiolate junction shown in the inset. Right: Effective potential at a bias voltage of 3 volts.

Let us finally mention some of the limitations of the DFT-based transport approach. It has recently been shown that the energetic position of molecular electronic levels at a solid-molecule interface can be substantially wrong in DFT due to self-interaction errors [90] and the lack of dynamical screening [91–93]. This circumstance is expected to influence the calculated conductance, in particular when the transport mechanism is off-resonant tunneling which is the most commonly encountered case. In such cases DFT must be considered to be only qualitatively correct while quantitative predictions require a many-body description such as the GW approximation [94]. More fundamental problems are encountered for weakly coupled and strongly correlated systems dominated by Coulomb blockade and Kondo physics where the single-particle approximation breaks down [95, 96]. In the opposite regime, characterized by strong molecule-lead couplings, DFT has been found to work surprisingly well and provides results in quantitative agreement with experiments [97, 98].

7 Additional features

7.1 Δ SCF

Δ SCF [33, 99, 100] is a simple method for estimating excitation energies within DFT. The acronym refers to the fact that the excitation energy is calculated as the difference between two self-consistent calculations, one traditional ground state calculation and one where an electron is constrained to a certain Kohn-Sham orbital as the system reaches self-consistency. The method is formally justified only when the constrained orbital is the lowest lying of its symmetry [101], but it is often applied in other situations with reasonable success [33, 102–105]. GPAW implements a generalized version of Δ SCF, where it is possible to constrain an electron to any linear combination of Kohn-Sham orbitals, which is desirable for molecules on surfaces where the molecular orbitals hybridizes with substrate states. A molecular orbital $|\alpha\rangle$ can always be represented by a linear combination of Kohn-Sham orbitals if a sufficient number of unoccupied Kohn-Sham orbitals is included in the calculation:

$$|\alpha\rangle = \sum_n c_n |\psi_n\rangle, \quad c_n = \langle \psi_n | \alpha \rangle. \quad (84)$$

The contribution to the PS electron density from this molecular orbital is then:

$$\Delta \tilde{n}_\alpha(\mathbf{r}) = \sum_{m,n} c_m^* c_n \tilde{\psi}_m^*(\mathbf{r}) \tilde{\psi}_n(\mathbf{r}), \quad (85)$$

and the corrections to the atomic density matrices Eq. (10) are

$$\Delta D_{i_1 i_2}^a = \sum_{m,n} c_m^* c_n \langle \tilde{\psi}_m | \tilde{p}_{i_1}^a \rangle \langle \tilde{p}_{i_2}^a | \tilde{\psi}_n \rangle.$$

The extra electron is usually taken from the Fermi level by simply requiring that the Fermi distribution integrates to the number of valence electrons minus one, but it is possible to introduce any specified hole according to the above description.

The contribution to the band energy from the excited state is given by

$$\langle \alpha | \hat{H} | \alpha \rangle = \sum_{m,n} c_m^* c_n \langle \psi_m | \hat{H} | \psi_n \rangle = \sum_n |c_n|^2 \varepsilon_n. \quad (86)$$

The linear combination in Eq. (84) is found by projecting the Kohn-Sham orbitals onto a desired orbital in the self-consistency cycle. In GPAW this can be done in the two different ways as described below.

7.1.1 Projector-pseudo wave function overlap

If the orbital to be kept occupied is an atomic orbital corresponding to a partial wave ($|\alpha\rangle = |\phi_i^a\rangle$), then the overlaps in Eq. (84) can be approximated by

$$\langle \psi_n | \phi_i^a \rangle \approx \langle \tilde{\psi}_n | \tilde{p}_i^a \rangle, \quad (87)$$

which follows from Eq. (5) if we neglect overlap between atomic sites. This is a quick and efficient way of obtaining the expansion coefficients c_n , since the projector overlaps Eq. (87) are calculated in each step of the self-consistence cycle anyway. The method is easily extended to molecular orbitals by taking appropriate linear combinations of $\langle \tilde{\psi}_n | \tilde{p}_i^a \rangle$.

7.1.2 AE wave function overlap

In principle one has access to the AE wave functions in the PAW formalism and thus it is possible to resolve any molecular orbital exactly into Kohn-Sham orbitals. However, the DFT PAW formalism works with the PS wave functions and these are the ones which are immediately available in the GPAW code.

To find the overlaps $c_n = \langle \psi_n | \alpha \rangle$ one should start by performing a gas-phase calculation of the molecule or atom which is to be used in an Δ SCF calculation. The PS wave function $|\tilde{\psi}_\alpha\rangle$ corresponding to the orbital to be occupied is then saved along with the its projector overlaps $\langle \tilde{p}_k^a | \tilde{\psi}_\alpha \rangle$ and the Δ SCF calculation is initialized. In each step of the calculation the AE overlap c_n can then be obtained by

$$c_n = \langle \psi_n | \psi_\alpha \rangle = \langle \tilde{\psi}_n | \tilde{\psi}_\alpha \rangle + \sum_{a, i_1, i_2} \langle \tilde{\psi}_n | \tilde{p}_{i_1}^a \rangle \Delta S_{i_1 i_2}^a \langle \tilde{p}_{i_2}^a | \tilde{\psi}_\alpha \rangle. \quad (88)$$

Note that there is only a single sum over atoms (and only the ones in the molecule) and that the cross terms of PS/AE wave functions do not contribute. Since the AE wave functions are orthonormal, the squared norm of the coefficients sums to one, $\sum_n |c_n|^2 = 1$, if the Kohn-Sham orbitals span the molecular orbital $|\alpha\rangle$. If this is not the case, one has to increase the number of unoccupied states in the calculation.

The expansion in Eq. (84) holds for each point in k-space so one has to use the same k-points in the gas phase calculation and then calculate the overlaps for each k-point.

7.1.3 Application to CO on Pt(111)

In Fig. 10 we show the potential energy surfaces of CO on a Pt surface (1/4 monolayer) in the ground state and in an excited state where the $2\pi^*$ resonance is occupied. This demonstrates how the minimum energy configuration in the resonance state is shifted with respect to the ground state, which is interesting in relation to molecular motion induced by hot electrons [102]. Fig. 10 also compares the projected density of states using the two projection methods described in Secs. 7.1.1 and 7.1.2 and clearly shows that the methods have the same qualitative features. However, the long high energy tail of the projector overlap method is a symptom of the lower accuracy of this method and indicates that the excitation energy will depend on the number of unoccupied bands included in the calculation. In contrast, the AE overlaps approaches zero for high lying states and this method can be converged in the number unoccupied bands. Finally, Fig. 10 shows the charge redistribution due to the excitation. The $2\pi^*$ orbital of the molecule is clearly seen as well as an induced image charge on the surface.

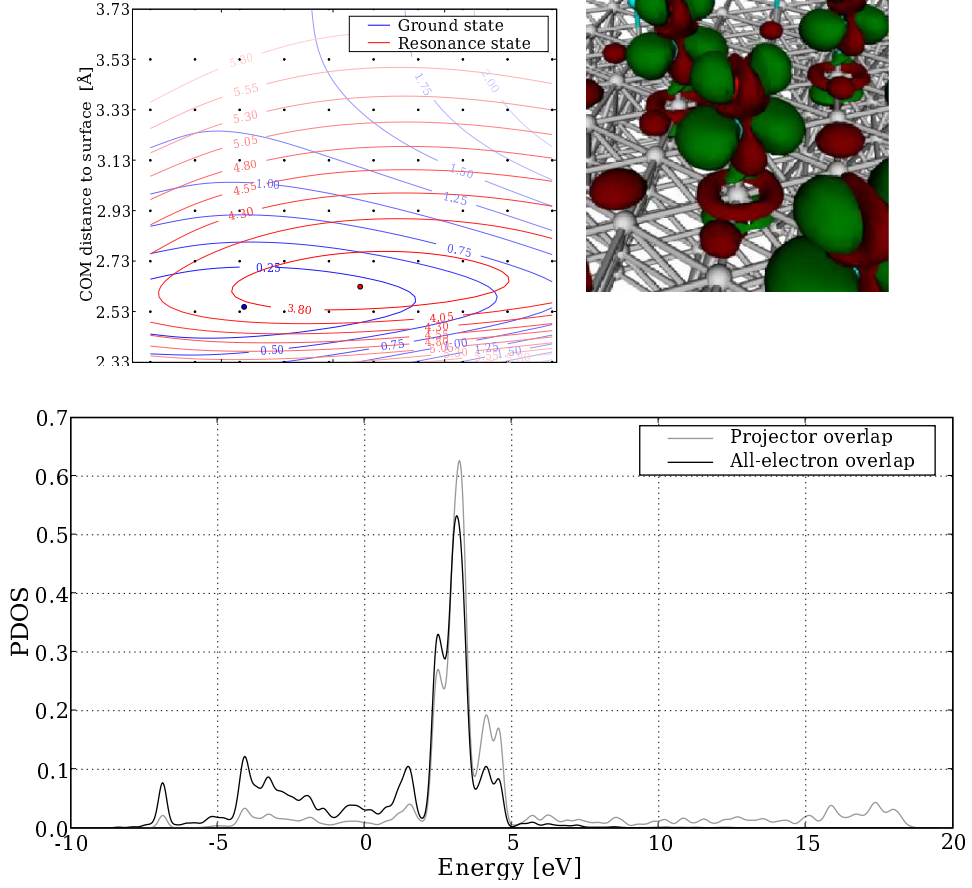


Figure 10: CO on Pt(111). Top left: Potential energy surfaces in the ground state and the $2\pi^*$ resonance as a function of the CO binding distance and the molecules center of mass distance to the surface. Top right: The change in charge distribution due to the excitation. Green: more charge (0.02 a.u. contour), red: less charge (-0.02 a.u. contour). Lower: Density of states projected onto the $2\pi^*$ orbital of CO using the two projection methods described in Secs. 7.1.1 and 7.1.2.

7.2 X-ray absorption spectra

In a one particle picture, X-ray absorption (XAS) can be viewed as exciting a core electron to an unoccupied orbital [106]. The absorption cross section is given by Fermi's golden rule:

$$\sigma(\omega) \propto \sum_f |\langle \psi_f | \mathbf{e} \cdot \boldsymbol{\mu} | \phi_c^a \rangle|^2 \delta(E_{fc} - \omega) \quad (89)$$

where $|\phi_c^a\rangle$ is the core orbital, $|\psi_f\rangle$ are unoccupied orbitals, E_{fc} is the eigenvalue difference between orbitals c and f , \mathbf{e} is the polarization vector of the incoming photon and $\boldsymbol{\mu}$ is the dipole operator. To account for core hole effects we use specially constructed PAW setups with half or a full electron removed from the core orbital. The wave functions are then relaxed in this potential [107]. Using the PAW transformation we can rewrite the

expression for the cross section [108]

$$\sigma(\omega) \propto \sum_f |\langle \tilde{\psi}_f | \tilde{\phi}_c^a \rangle|^2 \delta(E_{fc} - \omega) \quad (90)$$

where $|\tilde{\phi}_c^a\rangle = \sum_i |\tilde{p}_i^a\rangle \langle \phi_i^a | \mathbf{e} \cdot \boldsymbol{\mu} | \phi_c^a \rangle$. In the above expression for the cross section a lot of unoccupied states must be determined which is computationally demanding. This can be avoided with the Haydock recursion scheme [109] which we have also implemented. Due to the non-orthogonal PS wave functions in the PAW method the calculation of the recursion coefficients involves the inverse overlap \hat{S}^{-1} which cannot be explicitly computed. Instead, the equation $\hat{S}x = y$ is solved with the conjugate gradient method using an approximate \hat{S}^{-1} as a preconditioner [110]. The absolute energy scale is determined separately in a Δ SCF procedure where the total energy difference is computed between the ground state and the first core excited state using a full core hole setup and an extra electron in the valence band. Δ SCF transition energies depend strongly on the functional used [111], mostly due to differing descriptions of the core electrons. The spectra discussed in the following were calculated using the LDA functional, with the Δ SCF shifts computed using the BLYP functional.

In Fig. 11 we show the calculated half core hole XAS-spectrum for the pyridine nitrogen K-edge. A cubic box with 20 Å sides and a grid spacing of 0.2 Å was used with open boundary conditions. The agreement with experiment and a calculation using the StoBe code [112, 113] is good. Comparing the GPAW calculation to experiment the first peak is 0.8 eV too low and the relative energy between the first peak and the sigma resonance (408 eV in experiment) is about one electron volt too low.

Figure 11 shows also the calculated carbon K-edge XAS-spectrum of diamond both for half and full core hole. A cubic super cell with 216 atoms was used with periodic boundary conditions and the Brillouin zone was sampled at the Γ point. The grid spacing was set to 0.2 Å. The spectrum was calculated with the recursion method using $6 \times 6 \times 6$ k-points and 2000 recursion coefficients. The full core hole spectrum is in good agreement with [108], but has too much intensity near the onset of the spectrum compared to the experiment [114]. Neither the half or the full core hole reproduces the first excitonic peak of the experiment.

7.3 Wannier orbitals

The partly occupied maximally localized Wannier functions (WF) [115] are constructed by doing an unitary rotation for the lowest states (*fixed space*), and using a dynamically optimized linear combination of the remaining orbitals (*active space*). Both linear combinations are chosen such as to minimize the spread of the resulting Wannier functions. The unitarity of the rotation in the fixed spaces implies that the eigenvalues of the Bloch states contained in the fixed space can all be exactly reproduced by the resulting WF, whereas the largest eigenvalues of the WF will not necessarily correspond to any “real” eigenvalues.

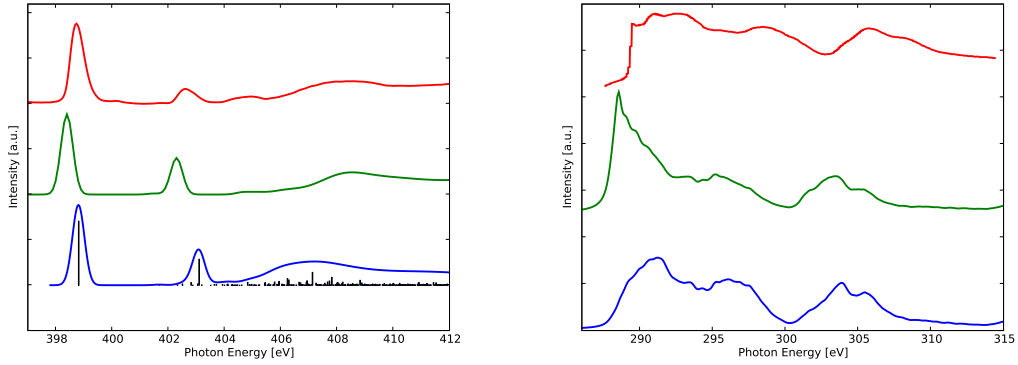


Figure 11: Left: Half core hole K-edge nitrogen spectrum of Pyridine. Spectrums shown are for GPAW (blue), StoBe (green), and experiment (red). The GPAW spectrum shows the individual oscillator strengths. Right: K-edge carbon spectrum of diamond. Spectrums shown are the half core hole (blue), full core hole (green), and experiment (red).

When constructing Wannier functions, the only quantities that need to be supplied from the DFT calculation are the integrals $Z_{n_1 n_2}^{\mathbf{G}} = \langle \psi_{n_1} | e^{-i\mathbf{G}\cdot\mathbf{r}} | \psi_{n_2} \rangle$, where \mathbf{G} is one of at most 6 possible (3 in an orthorhombic cell) vectors connecting nearest neighbor cells in the reciprocal lattice. When introducing the PAW transformation, this quantity can be expressed as [115, 116]

$$Z_{n_1 n_2}^{\mathbf{G}} = \langle \tilde{\psi}_{n_1} | e^{-i\mathbf{G}\cdot\mathbf{r}} | \tilde{\psi}_{n_2} \rangle \quad (91)$$

$$+ \sum_a \sum_{i_1 i_2} P_{i_1 n_1}^{a*} P_{i_2 n_2}^a \left(\langle \phi_{i_1}^a | e^{-i\mathbf{G}\cdot\mathbf{r}} | \phi_{i_2}^a \rangle - \langle \tilde{\phi}_{i_1}^a | e^{-i\mathbf{G}\cdot\mathbf{r}} | \tilde{\phi}_{i_2}^a \rangle \right). \quad (92)$$

Even for small systems, the phase of the exponential of the last integral does not vary significantly over the augmentation spheres where ϕ_i^a and $\tilde{\phi}_i^a$ differ. The integrals in the last two terms can therefore safely be approximated by taking the exponential outside the integrals as $e^{-i\mathbf{G}\cdot\mathbf{R}^a}$.

An example of partly occupied Wannier functions constructed using the GPAW code is shown in Fig. 12 (left) for a benzene molecule.

One can also, in the same sense as for the partly occupied Wannier functions, form a linear combination of the Kohn-Sham Bloch states, spanning the occupied space exactly, where the unitary rotation in the fixed space, and the linear combination of the active space are chosen such that the overlap of the resulting wave functions with the projector functions or the PS LCAO orbitals is maximized. This will result in a optimized single zeta numerical basis set, which can be used for minimal basis set calculations. An example of such localized optimized orbitals for benzene is shown in Fig. 12 (right). In this case the resulting orbitals have been rotated to diagonalize the Hamiltonian in the subspaces spanned by orbitals on the same atom. In GPAW, these functions are used as an efficient minimal basis set for performing computationally demanding GW calculations [52].

The algorithm for constructing such localized functions is much faster, and more robust

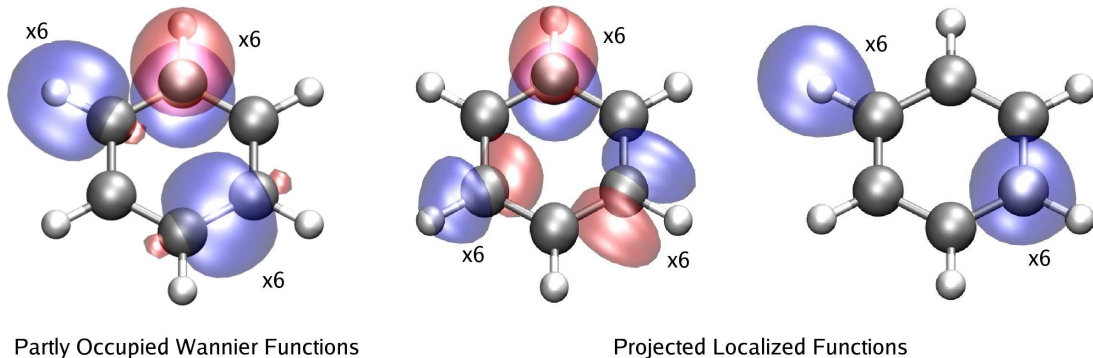


Figure 12: Left: Partly occupied WF; 6 C-H σ bonds, 6 C-C σ bonds, and 6 p_z orbitals on C. Right: Projected localized functions; 12 s orbitals on C and H respectively, and 3 p -type orbitals on each C, one p_z , one along the C-H bond, and one perpendicular to the C-H bond.

than the one for constructing the partly occupied WF, as it only involves some linear algebra on the pre-calculated projections, and not an iterative maximization of a spread functional. The procedure is described in more detail in Ref. [117].

An exact representation of the Kohn-Sham eigenstates in a minimal and maximally localized basis can facilitate orbital analysis [115].

7.4 Local properties

This section describes quantities that can somehow be related to a specific atom. As the PAW transform utilizes an inherent partitioning of space into atomic regions, such quantities are usually extractable from already determined atomic attributes, such as the atomic density matrices or the projector overlaps.

The projector overlaps P_{in}^a are simultaneous expansion coefficients of the PS and the AE wave functions inside the augmentation spheres (see Eqs. (5) – (6)). They can therefore be used both for reconstruction of AE wave function or densities, and for making a local expansion in atomic orbitals.

7.4.1 Density partitioning

Charge redistribution during a chemical reaction can often be studied by assigning the density distribution to the individual atoms. Formally, it is easy to reconstruct the true AE density from the PS density and the atom projected density matrix via Eq. (13).

In GPAW, charge assignment can be done in several ways. One choice is to apply a Wigner-Seitz scheme, where $\tilde{n}(\mathbf{r})$ at each grid point is assigned to the closest atom. The atomic PAW corrections in Eq. (13) can then be integrated on the radial grid, and added for each atom.

In the Bader analysis [118], it is not possible to apply the algorithm to the PS density and corrections separately, as the dividing surfaces might intersect the augmentation spheres.

Thus, the AE density should be reconstructed on a single regular grid, which can also be useful for other post-processing purposes. To accurately represent the peaked features of the AE density, the PS density is interpolated to a grid with reduced grid spacing before transferring the density corrections from the radial- to the uniform grid.

For the purpose of studying charge transfer, it can be advantageous to adjust the value of the atomic corrections on the uniform grid at the grid point closest to each nucleus, such that these integrate to the same value as on the more accurate radial grid. This does not affect the determination of the dividing surfaces, but enforces the integral properties of the reconstructed AE density within each domain.

In pseudopotential schemes, a reconstruction of the AE density is not possible, which can cause problems if dividing surfaces and pseudization regions intersect. This is the case for water, as illustrated in Fig. 13, showing the dividing surfaces of a water molecule determined using the Bader program [119] and the reconstructed AE density from GPAW.

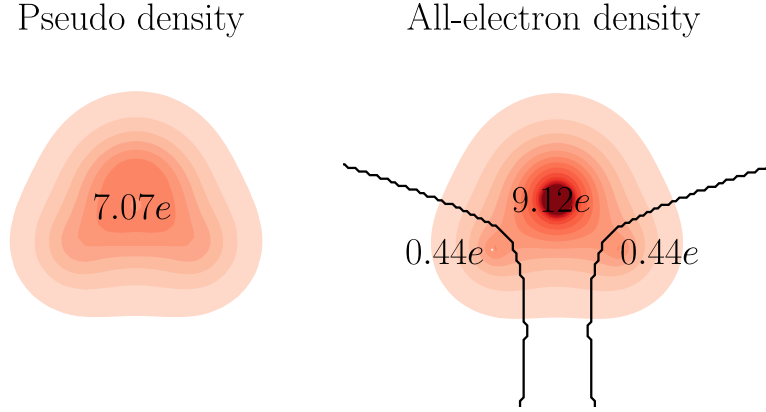


Figure 13: Contour lines for the PS (left) and reconstructed AE (right) densities of a water molecule. While the PS density only has a single maximum, the AE density has one distinct local maximum per atom, and a Bader partitioning scheme can be used to analyse charge transfer. The AE density integrates to the total number of electrons.

7.4.2 Projected density of states

Given a set of states $|\psi_n\rangle$ with eigenenergies ε_n , the density of states projected onto a state $|\alpha\rangle$ is defined by

$$\rho_\alpha(\varepsilon) = \sum_n |\langle \alpha | \psi_n \rangle|^2 \delta(\varepsilon - \varepsilon_n). \quad (93)$$

If $|\alpha\rangle$ is an atomic orbital which can be represented by a partial wave $|\phi_i^a\rangle$, the simplest way to obtain the overlaps is to use the single center expansion of the AE wave function Eq. (5), which gives $\langle \alpha | \psi_n \rangle \approx \langle \tilde{p}_i^a | \tilde{\psi}_n \rangle$ when neglecting the overlap of ϕ_i^a with neighbouring augmentation spheres. The method is easily extended to molecular orbitals by considering superpositions of partial waves.

If the state $|\alpha\rangle$ can be represented by a Kohn-Sham state $|\psi_\alpha\rangle$ from a different calculation, the PAW formalism allows one to obtain the AE overlaps exactly from Eq. (88). The

difference in the two methods is illustrated for the case of the $2\pi^*$ orbital of CO adsorbed on Pt(111) in Fig. 10. A major advantage of the AE overlap method is that the projected density of states is correctly normalized and one can obtain the fraction of an orbital located below a given energy by truncating the sum in Ref. (93) at that energy.

8 Parallel calculations

Drastic performance improvements in desktop computers and supercomputers are nowadays being achieved through new CPU designs with high density of processing elements (PEs). (Here we will use the terms cores, processors, and processing elements interchangeably). Thus, parallel computing is needed for utilizing this kind of hardware. The benefits of parallelization are two-fold: firstly, a reduction in the time-to-solution, and secondly, the capability to study larger problems. At present, parallelization of GPAW is accomplished using MPI; though with the advent of multicore CPUs fine-grained parallelism with OpenMP or Posix threads is a likely future enhancement.

The real-space representation allows seamless distribution of the PS wave function $\tilde{\psi}_{n\mathbf{k}\sigma}(\mathbf{r}_g)$ over all wave function indices: band n , \mathbf{k} -point, spin σ , as well as the grid-point g index. This is in sharp contrast to plane-wave basis codes which rely on the dual-space technique [120] for iterative diagonalization, and are thus complicated by representing the PS wave function in both real and reciprocal space. Parallelization over \mathbf{k} -points and spin is nearly trivial as these degrees are normally only coupled through electron density (except in the case of EXX). The generalized eigenvalue problem, Eq. (29) can be solved independently for each \mathbf{k} -point and spin. However, as there are significant number of \mathbf{k} -points only in small periodic systems and spin only in magnetic systems, the scalability accessible via \mathbf{k} -point and spin parallelization is limited benefit for large systems.

The primary parallelization scheme in GPAW is the domain decomposition of the real-space grid. The simulation box is divided among the PEs so that each subdomain has approximately the same number of grid points. Due to the local nature of the finite-difference Laplacian, communication is needed only between neighboring PEs when evaluating derivatives. The non-local parts of the PAW Hamiltonian also require only nearest-neighbor communication: Calculating an integral involving a projector function, $\langle \tilde{p}_i^a | \tilde{\psi}_n \rangle$, only involves contributions from those PEs that have grid points inside the augmentation sphere of atom a .

The computation of the dense matrix diagonalization and Cholesky decomposition needed for subspace diagonalization and orthogonalization scales as N_e^3 , where N_e is the number of electronic states. For large systems with many electrons ($N_e > 2000$), these operations can be excessively slow in serial and must be performed in a parallel. In GPAW, we use ScaLAPACK [121] to perform these dense linear algebra operations. In practice, a small subset of the PEs is used for ScaLAPACK parallelization. As an example, in a 2048 core calculation with $N_e \sim 1800$, ScaLAPACK diagonalizations is performed with only 16 cores and takes a few percent of the total computing time. In our most recent release of

GPAW, the associated dense linear algebra matrices, requiring $O(N_e^2)$ storage, are fully distributed so that very large problems $N_e > 10000$ can be treated.

Even though the real-space domain decomposition scales well, the ratio of computation to communication decreases when number of PEs is increased (for a fixed problem size). The limiting factor is the ratio N_g/P_d where N_g is the total number of grid points (proportional to system size N) and P_d is the number of PEs used for domain decomposition. The computational workload of the entire calculation scales as $O(N^3)$ (due to orthonormality constraints and subspace diagonalization), so that in large systems additional parallelization levels are necessary.

For large systems, domain-decomposition is combined with parallelization over the band index. This is ideal in the case of real-time propagation TDDFT because different electronic states can be propagated independently of each other and communication is needed only when summing for the electron density, similar to k-point and spin parallelization. However, for a ground-state DFT calculation, the subspace diagonalization and orthogonalization steps necessitate communication of all the electronic states on co-subdomains (g index). The amount of data to communicate per PE is proportional to $N_g N_e / (P_d P_e)$. On the other hand, the relevant computational workload is proportional to $N_g N_e^2 / (P_d P_e)$ (where P_e is the number of band groups and $P_d P_e$ equals to the total number of PEs). In sharp contrast to the domain decomposition, where the communication is proportional to surface area of the subdomain, parallelization over the band index introduces communication which is proportional to the *volume* of the subdomain. P_e must be carefully chosen so that the computation to communication ratio can be kept reasonable. Part of the communication overhead can often be hidden by overlapping communication and computation.

Optimal values of N_g/P_d and N_e/P_e depend a lot on the underlying hardware, but our experience has shown that typical minimum values are $N_g/P_d = 1000 - 8000$ and $N_e/P_e = 250$ for ground state calculations, and $N_e/P_e = 20 - 40$ for real-time propagation. This enables scaling to thousands of processors for large systems, as shown in Fig. 8. The ground-state DFT calculation is a 102 Au atom cluster surrounded by 44 p-MBA molecules [122] and the dimension of the system is ~ 3 nm. There are total of 762 atoms on 160^3 real-space grid and ~ 1800 electronic states are included in the calculation. The real-time propagation TDDFT is performed for a silicon cluster with 702 atoms on 160^3 real-space grid, the number of electronic states in the calculation is ~ 1600 .

When using the LCAO basis, the real-space domain decomposition is used when solving the Poisson equation and in the evaluation of two-center integrals. Dense matrix diagonalizations can also be performed with the help of ScaLAPACK, and parallelization over basis functions (equivalent of state parallelization in grid calculations) has been implemented. Generally, the parallel scaling of LCAO calculations is not as good as that of grid calculations, on the other hand the more modest memory requirement and computational workload enable large LCAO-type calculations with smaller number of CPUs.

In some special cases, it is possible to introduce further parallelization levels. For example,

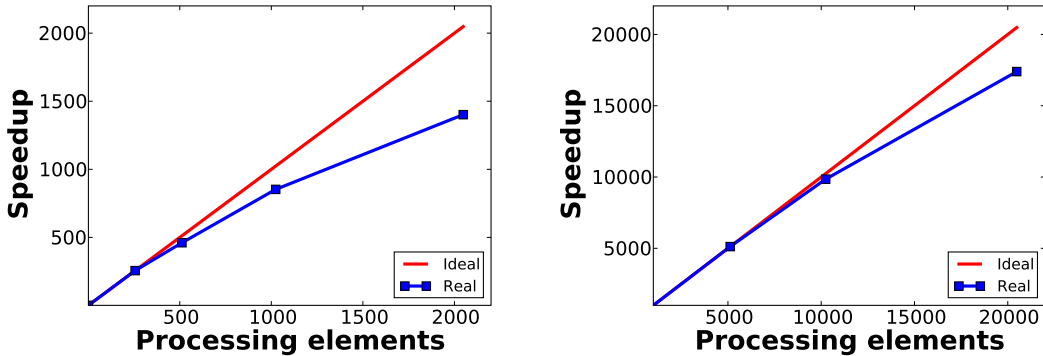


Figure 14: Parallel scaling for ground state total energy calculation (left) and for real-time propagation (right). The calculations are performed on a Cray XT5 systems at CSC and at Oak Ridge National Laboratory. The speedup is normalized so that at the first data point (256 PEs on left and 5000 PEs on right) the speed-up equals the number of PE's.

in nudged elastic band calculations the total energies of the images are independent and can hence be calculated in parallel. Also, when calculating optical spectra with real-time propagation the calculations over different polarization directions (if required by the symmetry of the system) can be performed in parallel. Finally, in linear response TDDFT the construction of the Ω matrix, Eq. (69), can be performed parallel over the electron-hole pairs. All these additional parallelization schemes are trivial and therefore scale ideally.

9 Summary and outlook

As described in this article, GPAW is now a stable and fairly mature real-space realization of DFT and TDDFT, based on the PAW method. In addition to the grid-based description, a localized atomic-orbital basis is available for fast computations of more limited accuracy. Many features have been implemented including a wide range of exchange-correlation functionals. The code is currently developed by an expanding group of developers situated primarily in Denmark, Finland, Sweden, and Germany with users from all over the world.

GPAW is an open-source project with only a loose organization behind it and therefore there exists no single long-term master plan for the further development of the code. The implementations that take place are exclusively based on the needs of the researchers working with the code and the whole project is therefore in the end carried by the enthusiasm of researchers at all levels. Among the features which are currently implemented, we mention the calculation of static response functions using density-functional perturbation theory and more general calculations of dynamical response functions within TDDFT. The calculation of forces as well as adiabatic and Ehrenfest dynamics are also being implemented within TDDFT. Furthermore, there is ongoing-work to extend the number of

atomic setups to include all elements through atomic number 86.

The GPAW code builds upon the Atomistic Simulation Environment (ASE) [123] which is a set of python modules to facilitate setting up, running, and analyzing atomistic/electronic calculations. The tight integration with ASE is expected to be maintained in the future. This seems natural also from the point of view that the interest in ASE has increased considerably the past few years so that ASE now supports about 12 different force and energy calculators.

There are of course a number of other open-source projects focused on DFT/TDDFT such as ABINIT, Quantum ESPRESSO, and Octopus. How does GPAW fit into this "market" of codes? The main feature which distinguishes GPAW is the combination of real-space description with the PAW method. The PAW allows for an accurate, essentially all-electron, frozen-core description which leads to soft pseudo wave functions even for transition metals. The real-space description allows for easy and very scalable parallelization through real-space decomposition making it possible to perform accurate calculations for large systems. Only time can tell which future developments will make their way into the GPAW code but almost certainly they will benefit from the PAW accuracy and the real-space parallelization.

10 Acknowledgements

This work has been supported by the Academy of Finland (Project 110013 and the Center of Excellence program) and Tekes MASI-program. We thank John Levesque from Cray Inc. for parallel calculations on the Cray XT5 Jaguar at Oak Ridge National Laboratory. The Argonne Leadership Computing Facility at Argonne National Laboratory is supported by the Office of Science of the U.S. Department of Energy under contract DE-AC02-06CH11357.

References

- [1] P. Hohenberg and W. Kohn. *Phys. Rev.*, **136**, B864–B871, 1964.
- [2] W. Kohn and L. J. Sham. *Phys. Rev.*, **140**, A1133–A1138, 1965.
- [3] Erich Runge and E. K. U. Gross. *Phys. Rev. Lett.*, **52**, 997 – 1000, 1984.
- [4] James C. Phillips and Leonard Kleinman. *Phys. Rev.*, **116**, 287–294, 1959.
- [5] Leonard Kleinman and D. M. Bylander. *Phys. Rev. Lett.*, **48**, 1425–1428, 1982.
- [6] David Vanderbilt. *Phys. Rev. B*, **41**, 7892–7895, 1990.
- [7] P. E. Blöchl. *Phys. Rev. B*, **50**, 17953–17979, 1994.

- [8] E. Wimmer, H. Krakauer, M. Weinert, and A. J. Freeman. *Phys. Rev. B*, **24**, 864–875, 1981.
- [9] M. C. Payne, M. P. Teter, D. C. Allan, T. A. Arias, and J. D. Joannopoulos. *Rev. Mod. Phys.*, **64**, 1045–1096, 1992.
- [10] W. J. Hehre, R. F. Stewart, and J. A. Pople. *J. Chem. Phys.*, **51**, 2657–2664, 1969.
- [11] José M Soler, Emilio Artacho, Julian D Gale, Alberto García, Javier Junquera, Pablo Ordejón, and Daniel Sánchez-Portal. *J. Phys.: Condens. Matter*, **14**, 2745, 2002.
- [12] Volker Blum, Ralf Gehrke, Felix Hanke, Paula Havu, Ville Havu, Xinguo Ren, Karsten Reuter, and Matthias Scheffler. *Comput. Phys. Commun.*, **180**, 2175 – 2196, 2009.
- [13] James R. Chelikowsky, N. Troullier, and Y. Saad. *Phys. Rev. Lett.*, **72**, 1240–1243, 1994.
- [14] T. L. Beck. *Rev. Mod. Phys.*, **72**, 1041, 2000.
- [15] Javier Junquera, Óscar Paz, Daniel Sánchez-Portal, and Emilio Artacho. *Phys. Rev. B*, **64**, 235111, 2001.
- [16] E. L. Briggs, D. J. Sullivan, and J. Bernholc. *Phys. Rev. B*, **54**, 14362–14375, 1996.
- [17] Eiji Tsuchida and Masaru Tsukada. *Phys. Rev. B*, **52**, 5573–5578, 1995.
- [18] J. E. Pask and P. A. Sterne. *Modelling Simul. Mater. Sci. Eng.*, **13**, R71–R96, 2005.
- [19] Lauri Lehtovaara, Ville Havu, and Martti Puska. *J. Chem. Phys.*, **131**, 054103, 2009.
- [20] <https://wiki.fysik.dtu.dk/gpaw>.
- [21] G. Kresse and D. Joubert. *Phys. Rev. B*, **59**, 1758, 1999.
- [22] X. Gonze, J.-M. Beuken, R. Caracas, F. Detraux, M. Fuchs, G.-M. Rignanese, L. Sindic, M. Verstraete, G. Zerah, F. Jollet, and M. Tor. *Comput. Mater. Sci.*, **25**, 478, 2002.
- [23] N. A. W. Holzwarth, G. E. Matthews, R. B. Dunning, A. R. Tackett, and Y. Zeng. *Phys. Rev. B*, **55**, 2005, 1997.
- [24] P. E. Blöchl, C. J. Först, and J. Schimpl. *Bull. Mat. Sci.*, **26**, 33, 2003.
- [25] G. Kresse and J. Furthmüller. *Comp. Mat. Sci.*, **6**, 15–50, 1996.

- [26] Paolo Giannozzi, Stefano Baroni, Nicola Bonini, Matteo Calandra, Roberto Car, Carlo Cavazzoni, Davide Ceresoli, Guido L Chiarotti, Matteo Cococcioni, Ismaila Dabo, Andrea Dal Corso, Stefano de Gironcoli, Stefano Fabris, Guido Fratesi, Ralph Gebauer, Uwe Gerstmann, Christos Gougoussis, Anton Kokalj, Michele Lazzeri, Layla Martin-Samos, Nicola Marzari, Francesco Mauri, Riccardo Mazzarello, Stefano Paolini, Alfredo Pasquarello, Lorenzo Paulatto, Carlo Sbraccia, Sandro Scandolo, Gabriele Scлаuzero, Ari P Seitsonen, Alexander Smogunov, Paolo Umari, and Renata M Wentzcovitch. *J. Phys.: Condens. Matter*, **21**, 395502 (19pp), 2009.
- [27] Reinhart Ahlrichs, Michael Bär, Marco Häser, Hans Horn, and Christoph Kölmel. *Chem. Phys. Lett.*, **162**, 165 – 169, 1989.
- [28] E. L. Briggs, D. J. Sullivan, and J. Bernholc. *Phys. Rev. B*, **52**, R5471–R5474, 1995.
- [29] M. A. L. Marques, Alberto Castro, George F. Bertsch, and Angel Rubio. *Comput. Phys. Commun.*, **151**, 60–78, 2003.
- [30] M. Heiskanen, T. Torsti, M.J. Puska, and R.M. Nieminen. *Phys. Rev. B*, **63**, 245106, 2001.
- [31] K. Yabana and G. F. Bertsch. *Phys. Rev. B*, **54**, 4484, 1996.
- [32] M. E. Casida. Time-dependent density functional response theory of molecular systems: Theory, computational methods, and functionals. In J. M. Seminario, editor, *Recent Developments and Applications in Modern Density-Functional Theory*, page 391. Elsevier, Amsterdam, 1996.
- [33] J. Gavnholt, T. Olsen, M. Engelund, and J. Schiøtz. *Phys. Rev. B*, **78**, 075441, 2008.
- [34] J.J. Mortensen, Hansen L. B., and K.W. Jacobsen. *Phys. Rev. B*, **71**, 035109, 2005.
- [35] Adam Kiejna, Georg Kresse, Jutta Rogal, Abir De Sarkar, Karsten Reuter, and Matthias Scheffler. *Phys. Rev. B*, **73**, 035404, 2006.
- [36] Amir Natan, Ayelet Benjamini, Doron Naveh, Leeor Kronik, Murilo L. Tiago, Scott P. Beckman, and James R. Chelikowsky. *Phys. Rev. B*, **78**, 075109, 2008.
- [37] Maxim Tafipolsky and Rochus Schmid. *J. Comp. Phys.*, **124**, 174102, 2006.
- [38] C. Hartwigsen, S. Goedecker, and J. Hutter. *Phys. Rev. B*, **58**, 3641–3662, 1998.
- [39] G. Kresse and J. Furthmüller. *Phys. Rev. B*, **54**, 11169–11186, 1996.
- [40] D. M. Wood and A. Zunger. *J. Phys. A: Math. Gen.*, **18**, 1343, 1985.
- [41] Y. T. Feng and D. R. J. Owen. *Int. J. Num. Meth. in Engineer.*, **39**, 2209–2229, 1996.

- [42] Ernest R. Davidson. *J. Comp. Phys.*, **17**, 87–94, 1975.
- [43] Peter Pulay. *Chem. Phys. Lett.*, **73**, 393–398, 1980.
- [44] <http://www.tddft.org/programs/octopus/wiki/index.php/Libxc>.
- [45] John P. Perdew, Adrienn Ruzsinszky, Jianmin Tao, Viktor N. Staroverov, Gustavo E. Scuseria, and Gábor I. Csonka. *J. Chem. Phys.*, **123**, 062201, 2005.
- [46] Jianmin Tao, John P. Perdew, Viktor N. Staroverov, and Gustavo E. Scuseria. *Phys. Rev. Lett.*, **91**, 146401, 2003.
- [47] Yan Zhao and Donald G. Truhlar. *J. Chem. Phys.*, **125**, 194101, 2006.
- [48] John P. Perdew, Adrienn Ruzsinszky, Gabor I. Csonka, Lucian A. Constantin, and Jianwei Sun. *Phys. Rev. Lett.*, **103**, 2009.
- [49] J. P. Perdew, J. Tao, V. N. Staroverov, and G. Scuseria. *J. Chem. Phys.*, **120**, 6898–6911, 2004.
- [50] J Paier, R. Hirschl, M. Marsman, and Kresse G. *J. Chem. Phys.*, **122**, 234102, 2005.
- [51] Michael Walter, Hannu Häkkinen, Lauri Lehtovaara, Martti Puska, Jussi Enkovaara, Carsten Rostgaard, and Jens Jørgen Mortensen. *J. Chem. Phys.*, **128**, 244101, 2008.
- [52] C. Rostgaard, K. W. Jacobsen, and K. S. Thygesen. *Phys. Rev. B*, **81**, 085103, 2010.
- [53] S. Massidda, M. Posternak, and A. Baldereschi. *Phys. Rev. B*, **48**, 5058–5068, 1993.
- [54] Carsten Rostgaard. The projector augmented-wave method. arXiv:0910.1921 [cond-mat.mtrl-sci], 2009.
- [55] C. Adamo and V. Barone. *J. Chem. Phys.*, **110**, 6158–6170, 1999.
- [56] Larry A. Curtiss, Krishnan Raghavachari, Paul C. Redfern, and John A. Pople. *J. Chem. Phys.*, **106**, 1063–1079, 1997.
- [57] Oleg Gritsenko, Robert van Leeuwen, Erik van Lenthe, and Evert Jan Baerends. *Phys. Rev. A*, **51**, 1944–1954, 1995.
- [58] A. D. Becke. *Phys. Rev. A*, **38**, 3098–3100, 1988.
- [59] Mikael Kuisma, Jussi Ojanen, Jussi Enkovaara, and Tapio T. Rantala. submitted, 2010.
- [60] John P. Perdew, Adrienn Ruzsinszky, Gábor I. Csonka, Oleg A. Vydrov, Gustavo E. Scuseria, Lucian A. Constantin, Xiaolan Zhou, and Kieron Burke. *Phys. Rev. Lett.*, **100**, 136406, 2008.
- [61] John P. Perdew and Mel Levy. *Phys. Rev. Lett.*, **51**, 1884–1887, 1983.

- [62] L. J. Sham and M. Schlüter. *Phys. Rev. Lett.*, **51**, 1888–1891, 1983.
- [63] M. Levinshtein, S. Rumyantsev, and M. Shur. *Handbook series on Semiconductor Parameters*. World Scientific, 1996.
- [64] M. Dion, H. Rydberg, E. Schroder, D. C. Langreth, and B. I. Lundqvist. *Phys. Rev. Lett.*, **92**, 246401, 2004.
- [65] M. Dion, H. Rydberg, E. Schröder, D. C. Langreth, and B. I. Lundqvist. *Phys. Rev. Lett.*, **92**, 246401, 2004.
- [66] Guillermo Román-Pérez and José M Soler. *Phys. Rev. Lett.*, **103**, 096102, 2009.
- [67] J. Wellendorff, A. Kelkkanen, J. J. Mortensen, B. I. Lundqvist, and T. Bligaard. *Topics in Catalysis, Online First*, 2010.
- [68] S. L. Dudarev, G. A. Botton, S. Y. Savrasov, C. J. Humphreys, and A. P. Sutton. *Phys. Rev. B*, **57**, 1505–1509, 1998.
- [69] A. Rohrbach, J. Hafner, and G. Kresse. *Phys. Rev. B*, **69**, 075413, 2004.
- [70] Thomas Maxisch Lei Wang and Gerbrand Ceder. *Phys. Rev. B*, **73**, 195107, 2006.
- [71] Fabien Tran, Peter Blaha, Karlheinz Schwarz, and Pavel Novák. *Phys. Rev. B*, **74**, 155108, 2006.
- [72] J. J. Mortensen, K. Kaasbjerg, S. L. Frederiksen, J. K. Nørskov, J. P. Sethna, and K. W. Jacobsen. *Phys. Rev. Lett.*, **95**, 216401, 2005.
- [73] John P. Perdew, Kieron Burke, and Matthias Ernzerhof. *Phys. Rev. Lett.*, **77**, 3865–3868, 1996.
- [74] K. Yabana and G. F. Bertsch. *Int. J. Quantum Chem.*, **75**, 55 – 66, 1999.
- [75] M.E. Casida. Time-dependent density-functional response theory for molecules. In D.P. Chong, editor, *Recent Advances in Density Functional Methods, Part I*, page 155. World Scientific, Singapore, 1995.
- [76] T. Grabo, M. Petersilka, and E. K. U. Gross. *Journal of Molecular Structure: THEOCHEM*, **501-502**, 353 – 367, 2000.
- [77] Y. Negishi, N. K. Chaki, R. L. Whetten, and T. Tsukuda. *J. Am. Chem. Soc.*, **129**, 11322, 2007.
- [78] Daniel Neuhasuer and Michael Baer. *J. Chem. Phys.*, **90**, 4351–4355, 1989.
- [79] D. P. Chong, O. V. Gritsenko, and E. J. Baerends. *J. Chem. Phys.*, **116**, 1760–1772, 2002.
- [80] Michael Walter and Hannu Häkkinen. *New J. Phys.*, **10**, 043018 (10pp), 2008.
- [81] D. A. Allison and Cavell R. G. *J. Chem. Phys.*, **68**, 593–601, 1978.

- [82] A. H. Larsen, M. Vanin, J. J. Mortensen, K. S. Thygesen, and K. W. Jacobsen. *Phys. Rev. B*, **80**, 195112, 2009.
- [83] D. J. Niklewski O. F. Sankey. *Phys. Rev. B*, **40**, 3979, 1989.
- [84] E. Anglada, J. M. Soler, J. Junquera, and E. Artacho. *Phys. Rev. B*, **66**, 205101, 2002.
- [85] F. Guinea, C. Tejedor, F. Flores, and E. Louis. *Phys. Rev. B*, **28**, 4397, 1983.
- [86] M. Brandbyge, J. L. Mozos, P. Ordejón, J. Taylor, and K. Stokbro. *Phys. Rev. B*, **65**, 165401, 2002.
- [87] T. N. L. Patterson. *Math. Comput.*, **22**, 847, 1968.
- [88] Y. Meir and N. S. Wingreen. *Phys. Rev. B*, **68**, 2512, 1992.
- [89] K. S. Thygesen. *Phys. Rev. B*, **73**, 035309, 2006.
- [90] Toher C. and Sanvito S. *Phys. Rev. B*, **77**, 155402, 2008.
- [91] Neaton J. B., Hybertsen M. S., and Louie S. G. *Phys. Rev. Lett.*, **97**, 216405, 2006.
- [92] Garcia-Lastra J. M., Rostgaard C., Rubio A., and Thygesen K. S. *Phys. Rev. B*, **80**, 245427, 2009.
- [93] Thygesen K. S. *Phys. Rev. Lett.*, **100**, 166804, 2008.
- [94] Thygesen K. S. and Rubio A. *Phys. Rev. B*, **77**, 115333, 2008.
- [95] X. Wang, C. D. Spataru, M. S. Hybertsen, and A. J. Millis. *Phys. Rev. B*, **77**, 045119, 2008.
- [96] D. Jacob, K. Haule, and Kotliar G. *Phys. Rev. Lett.*, **103**, 016803, 2009.
- [97] E. Scheer, N. Agrait, J. C. Cuevas, A. L. Yeyati, B. Ludoph, A. Martin-Rodero, G. R. Bollinger, J. M. van Ruitenbeek, and C. Urbina. *Nature*, **394**, 154–157, 1998.
- [98] D. Djukic, K. S. Thygesen, C. Untiedt, R. H. M. Smit, K. W. Jacobsen, and J. M. van Ruitenbeek. *Phys. Rev. B*, **71**, 161402, 2005.
- [99] R. O. Jones and O. Gunnarsson. *Rev. Mod. Phys.*, **61**, 689–746, 1989.
- [100] A. Hellman, B. Razaznejad, and B. I. Lundqvist. *J. Chem. Phys.*, **120**, 4593–4602, 2004.
- [101] O. Gunnarsson and B. I. Lundqvist. *Phys. Rev. B*, **13**, 4274–4298, 1976.
- [102] T. Olsen, J. Gavnholt, and J. Schiøtz. *Phys. Rev. B*, **79**, 035403, 2009.
- [103] T. Olsen. *Phys. Rev. B*, **79**, 235414, 2009.
- [104] T. Olsen and J. Schiøtz. *Phys. Rev. Lett*, **103**, 238301, 2009.

- [105] T. Olsen and J. Schiøtz. *Phys. Rev. B*, **81**, 115443, 2010.
- [106] Joachim Stöhr. *NEXAFS Spectroscopy*. Springer, 1992.
- [107] L. Triguero, L. G. M. Pettersson, and H. Ågren. *Phys. Rev. B*, **58**, 8097–8110, 1998.
- [108] Mathieu Taillefumier, Delphine Cabaret, Anne-Marie Flank, and Francesco Mauri. *Phys. Rev. B*, **66**, 195107, 2002.
- [109] R Haydock, V Heine, and M J Kelly. *J. Phys. C: Solid State Phys.*, **5**, 2845–2858, 1972.
- [110] P.J. Hasnip and C.J Pickard. *Comp. Phys. Comm*, **174**, 24–29, 2006.
- [111] Osamu Takahashi and Lars G. M. Pettersson. *J. Chem. Phys.*, **121**, 10339–10345, 2004.
- [112] C. Kolczewski, R. Püttner, O. Plashkevych, H. Ågren, V. Staemmler, M. Martins, G. Snell, A. S. Schlachter, M. Sant’Anna, G. Kaindl, and L. G. M. Pettersson. *J. Chem. Phys.*, **115**, 6426–6437, 2001.
- [113] <http://w3.rz-berlin.mpg.de/~hermann/StoBe/>.
- [114] Y. Ma, N. Wassdahl, P. Skytt, J. Guo, J. Nordgren, P. D. Johnson, J-E. Rubensson, T. Boske, W. Eberhardt, and S. D. Kevan. *Phys. Rev. Lett.*, **69**, 2598–2601, 1992.
- [115] K. S. Thygesen, L. B. Hansen, and K. W. Jacobsen. *Phys. Rev. B*, **72**, 125119, 2005.
- [116] A Ferretti, A Calzolari, B Bonferroni, and R Di Felice. *J. Phys.: Condens. Matter*, **19**, 036215 (16pp), 2007.
- [117] Su Ying Quek, Latha Venkataraman, Hyoung Joon Choi, Steven G. Louie, Mark S. Hybertsen, and J. B. Neaton. *Nano Letters*, **7**, 3477–3482, 2007.
- [118] W. Tang, E. Sanville, and G. Henkelman. A grid-based bader analysis algorithm without lattice bias. In press, *J. Phys.: Condens. Matter*, 2008.
- [119] <http://theory.cm.utexas.edu/henkelman/research/bader/>.
- [120] J. L. Martins and M. L. Cohen. *Phys. Rev. B*, **37**, 6134, 1988.
- [121] L. S. Blackford, J. Choi, A. Cleary, E. D’Azevedo, J. Demmel, I. Dhillon, J. Dongarra, S. Hammarling, G. Henry, A. Petitet, K. Stanley, D. Walker, and R. C. Whaley. *ScaLAPACK Users’ Guide*. Society for Industrial and Applied Mathematics, Philadelphia, PA, 1997.
- [122] Michael Walter, Jaakko Akola, Olga Lopez-Acevedo, Pablo D. Jadzinsky, Guillermo Calero, Christopher J. Ackerson, Robert L. Whetten, Henrik Grönbeck, and Hannu Häkkinen. *PNAS*, **105**, 9157–9162, 2008.

[123] <https://wiki.fysik.dtu.dk/ase>.